Nano Research

ISSN 1998-0124 CN 11-5974/O4
https://doi.org/10.26599/NR.2026.94909213

Research Article

Asymmetric CoSn coordination-induced Fenton-like reaction

Zheng Liu[1], Jinlong Ge[2], Xuhua Li[1], Xiaoxin Li[1], Jiuli Ruan[1], Ruonan Zhao[1], Han Wang[1], Ting Cao[1], Haiyang Lv[1], Yao Zhu[1], Xin Xia[3], Bingbing Huang[3], Qian Bai[3], Xiaolu Ma[3], Rui Yang[3], Zhengbang Zhu[3], Jilin Li[3], Jingqiao Zhang[1](✉), Shuai Li[4,5](✉), Yan Gao[2](✉)

[1] State Key Laboratory of Environmental Criteria and Risk Assessment, key Laboratory of Eco-industry of Ministry of Ecology and Environment, Chinese Research Academy of Environmental Sciences, Beijing 100012, China

[2] Anhui Provincial Engineering Research Center of Silicon-based Materials, Bengbu University, Bengbu 233030, China

[3] Energy & Catalysis Center, School of Materials Science and Engineering, Beijing Institute of Technology, Beijing 100081, China

[4] School of Marine Engineering, Xiamen Ocean Vocational College, Xiamen 361012, China

[5] College of Environmental Science and Engineering, North China Electric Power University, Beijing 102206, China

Nano Res., **Just Accepted Manuscript** • https://doi.org/10.26599/NR.2026.94909213

https://www.sciopen.com/journal/1998-0124 on Sep. 23, 2026

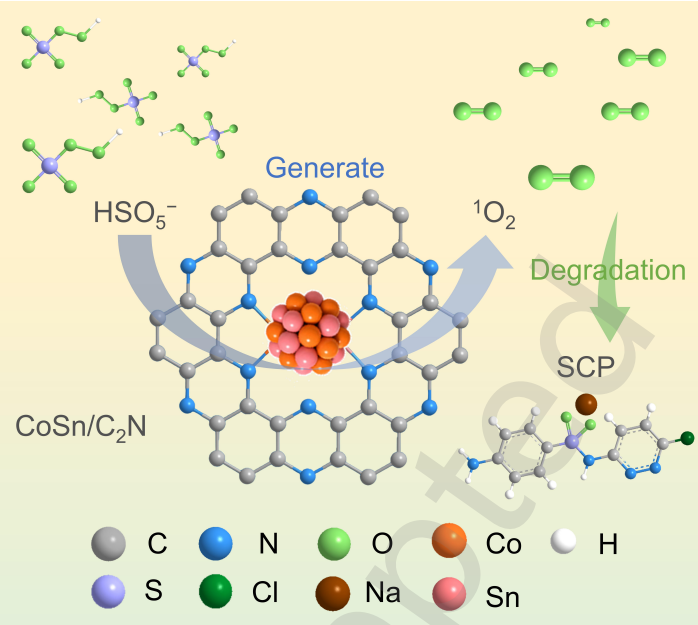
© The Authors(s)

Just Accepted

This is a "Just Accepted" manuscript, which has been examined by the peer-review process and has been accepted for publication. A "Just Accepted" manuscript is published online shortly after its acceptance,which is prior to technical editing and formatting and author proofing. Tsinghua University Press (TUP) provides "Just Accepted" as an optional and free service which allows authors to make their results available to the research community as soon as possible after acceptance. After a manuscript has been technically edited and formatted, and the page proofs have been corrected, it will be removed from the "Just Accepted" web site and published officially with volume and article number (e.g., *Nano Research*, **2025**, *18*, 94906990). Please note that technical editing may introduce minor changes to the manuscript text and/or graphics which may affect the content, and all legal disclaimers that apply to the journal pertain. In no event shall TUP be held responsible for errors or consequences arising from the use of any information contained in these "Just Accepted" manuscripts. To cite this anuscript please use its Digital Object Identifier (DOI®),which is identical for all formats of publication.

Just Accepted

TABLE OF CONTENTS (TOC)



Ultrasmall CoSn bimetallic sites coordinated with the N-rich C_2N framework create an asymmetric electronic environment for efficient PMS activation. The resulting $CoSn/C_2N$ catalyst enables rapid sulfachloropyridazine degradation through a dominant $^1O_2$-mediated nonradical pathway.

Just Accepted

Nano Research

Open Access

Research Article

Asymmetric CoSn coordination-induced Fenton-like reaction

Zheng Liu[1], Jinlong Ge[2], Xuhua Li[1], Xiaoxin Li[1], Jiuli Ruan[1], Ruonan Zhao[1], Han Wang[1], Ting Cao[1], Haiyang Lv[1], Yao Zhu[1], Xin Xia[3], Bingbing Huang[3], Qian Bai[3], Xiaolu Ma[3], Rui Yang[3], Zhengbang Zhu[3], Jilin Li[3], Jingqiao Zhang[1,*], Shuai Li[4,5,*], Yan Gao[2,*]

[1] State Key Laboratory of Environmental Criteria and Risk Assessment, key Laboratory of Eco-industry of Ministry of Ecology and Environment, Chinese Research Academy of Environmental Sciences, Beijing 100012, China
[2] Anhui Provincial Engineering Research Center of Silicon-based Materials, Bengbu University, Bengbu 233030, China
[3] Energy & Catalysis Center, School of Materials Science and Engineering, Beijing Institute of Technology, Beijing, 100081, China
[4] School of Marine Engineering, Xiamen Ocean Vocational College, Xiamen 361012, China[5] College of Environmental Science and Engineering, North China Electric Power University, Beijing 102206, China

Received: 15 July 2026; **Revised:** 6 September 2026; **Accepted:** 23 September 2026

Address correspondence to Jingqiao Zhang, zhangjq@craes.org.cn; Shuai Li, lishuai@163.com; Yan Gao, gaoyan@bbc.edu.cn

Cite this article: *Nano Research*, 2026, 19, 94909213 https://doi.org/10.26599/NR.2026.94909213

ABSTRACT: Precise construction of asymmetric bimetallic coordination sites is important for developing efficient Fenton-like catalysts, but stabilizing such structures on nitrogen-rich carbon supports remains challenging. Herein, an ultrasmall CoSn particle-supported C_2N catalyst (CoSn/C_2N) was prepared through a supramolecular assembly-assisted pyrolysis strategy using melamine, cyanuric acid, CoPc, SnPc, and oxalic acid as precursors. The obtained CoSn/C_2N exhibited a flower-like architecture assembled from ultrathin wrinkled nanosheets, with highly dispersed CoSn particles mainly distributed at 1.0–1.2 nm. XANES, EXAFS fitting, and WT-EXAFS analyses revealed the partially oxidized states of Co and Sn, confirmed Co–Sn coordination, and demonstrated strong coupling between the bimetallic particles and the C_2N. Benefiting from this unique local structure, CoSn/C_2N efficiently activated peroxymonosulfate for sulfachloropyridazine degradation, achieving complete removal within 10 min with an apparent rate constant of 0.25 min^{-1}, higher than those of Co/C_2N and Sn/C_2N. The CoSn/C_2N/PMS system maintained high activity over a broad pH range, resisted interference from common ions and humic acid, and retained complete removal after five cycles. Quenching experiments and EPR spectra identified singlet oxygen as the dominant reactive species, indicating a $^1O_2$-mediated nonradical oxidation pathway. This work provides a feasible strategy for designing C_2N-confined bimetallic catalysts for antibiotic wastewater treatment.

KEYWORDS: asymmetric coordination; C_2N; High-efficiency activation; Fenton-like reaction

1 Introduction

Antibiotic residues in aquatic environments have become an increasingly serious environmental issue because of their continuous discharge, biological persistence, and potential contribution to the spread of antibiotic resistance[1,7,11]. Large amounts of antibiotics are used in pharmaceutical production, livestock breeding, aquaculture, and clinical treatment, but a considerable fraction cannot be fully metabolized and is released into wastewater streams[2-6]. Among various antibiotic contaminants, sulfonamides are frequently detected in pharmaceutical and livestock wastewater due to their broad-spectrum antibacterial activity, high consumption, and relatively stable molecular structures[8-10]. Sulfachloropyridazine (SCP), as a representative sulfonamide antibiotic, contains electron-rich aromatic rings, sulfonamide groups, and heterocyclic structures, which make it resistant to conventional biological treatment. Even at trace concentrations, residual SCP may induce ecological risks and promote the development of resistant microorganisms. Therefore, developing efficient and reliable treatment technologies for SCP-containing wastewater is of great importance. Advanced oxidation processes (AOPs) have attracted extensive attention because they can generate highly reactive oxygen species capable of decomposing refractory organic pollutants[12-15]. In particular, peroxymonosulfate (PMS)-based oxidation systems have been widely investigated owing to their high oxidation potential, broad pH adaptability, and relatively easy activation under mild conditions. However, the efficiency and selectivity of PMS activation strongly depend on the structure and electronic properties of the catalyst.[16-17] Therefore, designing advanced catalysts with well-defined active sites and controllable reaction pathways remains essential for improving antibiotic degradation.

Transition-metal-based Fenton-like catalysts are among the most effective materials for PMS activation because transition-metal sites can mediate electron transfer and promote the cleavage or transformation of PMS. Conventional PMS activation systems are usually associated with the generation of sulfate radicals and hydroxyl radicals, which possess strong oxidation ability toward various organic pollutants[18-21]. Nevertheless, radical-dominated pathways often suffer from several limitations in practical water

Just Accepted

treatment. For example, radical species are short-lived, poorly selective, and easily consumed by coexisting inorganic ions, natural organic matter, and background water matrices[22]. These side reactions reduce the effective utilization of oxidants and may weaken pollutant degradation in real wastewater. Recently, nonradical PMS activation pathways have emerged as attractive alternatives. Among them, singlet oxygen-mediated oxidation has received increasing attention because singlet oxygen exhibits relatively high selectivity, better resistance to common water constituents[23-27], and lower dependence on strongly acidic conditions. The formation of singlet oxygen is closely related to the surface electronic structure, local coordination environment, and interfacial electron-transfer behavior of catalysts. In this regard, bimetallic catalysts provide an effective platform for tuning PMS activation pathways[28-30]. Compared with monometallic catalysts, bimetallic systems can create metal–metal interactions, redistribute electron density, and generate asymmetric coordination environments. Such structural features may modify PMS adsorption and activation behavior, thereby regulating the generation of reactive oxygen species[31-33]. However, bimetallic nanoparticles are prone to aggregation during high-temperature synthesis, which reduces the exposure of active sites and weakens structural stability. Constructing ultrasmall bimetallic particles within a confined nitrogen-rich carbon framework is therefore a promising strategy to improve metal dispersion and stabilize active coordination structures [34, 51-52].

C_2N, as a nitrogen-rich two-dimensional carbon material, provides a unique platform for anchoring metal species because of its abundant nitrogen sites[35-36, 53], ordered porous structure, and strong metal–support interactions. The electron-rich nitrogen atoms in C_2N can coordinate with metal centers, restrict particle growth, and modulate the local electronic structure of supported metal species. These characteristics make C_2N suitable for constructing confined bimetallic catalysts with well-dispersed active sites [54-55]. Inspired by this, herein we developed an ultrasmall CoSn particle-supported C_2N catalyst through a supramolecular assembly-assisted pyrolysis strategy. Melamine and cyanuric acid were used as nitrogen-rich precursors to form a hydrogen-bonded supramolecular framework, while cobalt phthalocyanine and tin phthalocyanine served as Co and Sn sources. Oxalic acid was introduced as an auxiliary component to assist morphology regulation and precursor assembly. After pyrolysis, ultrasmall CoSn particles were uniformly anchored on a flower-like C_2N-derived nanosheet framework[37]. Structural characterizations revealed homogeneous Co/Sn distribution, narrow particle-size distribution, partially oxidized Co and Sn species, and clear Co–Sn coordination, confirming the formation of a distinct bimetallic local structure rather than separated metal or oxide phases. The catalytic behavior of CoSn/C_2N was evaluated by PMS activation toward SCP degradation, with Co/C_2N and Sn/C_2N used as comparison samples[38]. In addition, quenching experiments and electron paramagnetic resonance measurements were performed to identify the dominant reactive oxygen species and clarify the oxidation mechanism. This work aims to reveal the role of C_2N-confined CoSn bimetallic coordination in regulating PMS activation and provides a feasible strategy for designing nonradical Fenton-like catalysts for antibiotic wastewater treatment[39-40].

2 Results and discussion

2.1 Morphology and structure analysis of catalysts

Melamine and cyanuric acid were employed as nitrogen-rich precursors to construct a hydrogen-bonded supramolecular assembly through molecular self-organization. During thermal treatment, melamine and cyanuric acid undergo condensation and polymerization reactions, providing a carbon nitride-like framework enriched with nitrogen coordination sites[41]. In this synthesis, cobalt phthalocyanine (CoPc) and tin phthalocyanine (SnPc) were introduced as metal-containing molecular precursors, while oxalic acid was used as an auxiliary carbon source and structure-regulating agent. These components were uniformly mixed in solvent to form a homogeneous supramolecular intermediate, in which the metal centers and nitrogen-containing organic building blocks were spatially integrated at the molecular level.

Subsequent pyrolysis of the supramolecular intermediate at 850 °C under an argon atmosphere promoted the carbonization of the organic precursors and the in situ construction of Co/Sn-containing nitrogen-doped carbon materials. During this process, the nitrogen-rich framework derived from melamine and cyanuric acid provided abundant coordination sites for anchoring metal species, while the planar macrocyclic structures of CoPc and SnPc facilitated the homogeneous dispersion of Co and Sn species within the carbon matrix. Meanwhile, oxalic acid contributed to the regulation of the porous and layered morphology by participating in carbonization and gas-releasing decomposition during pyrolysis. As illustrated in Figure 1, the integrated supramolecular assembly strategy enables the formation of a hierarchically stacked, flower-like carbon architecture with highly dispersed Co/Sn-related active sites. (Fig. 1(a))

Just Accepted

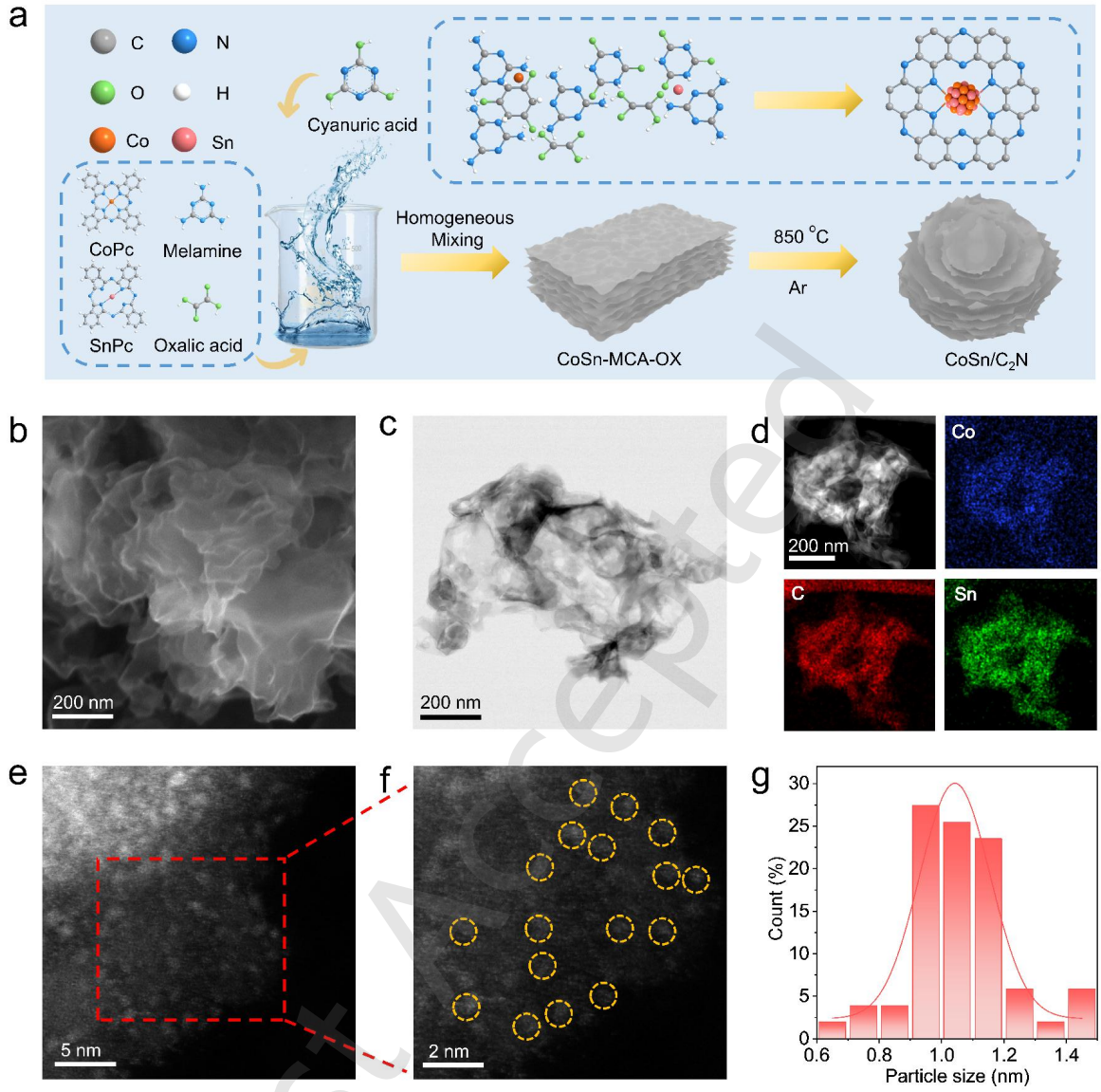


Figure 1 (a) Schematic illustration of the synthesis process of $CoSn/C_2N$. (b) SEM image of $CoSn/C_2N$. (c) TEM image of $CoSn/C_2N$. (d) HAADF-STEM image and corresponding elemental mapping images of $CoSn/C_2N$. (e) HAADF-STEM image of $CoSn/C_2N$. (f) Enlarged HAADF-STEM image of CoSn particles anchored on C_2N. (g) Particle size CoSn particles of the $CoSn/C_2N$.

As displayed in Fig. 1(b) and Fig. S1 and S2 in the Electronic Supplementary Material (ESM), the sample exhibits a three-dimensional flower-like architecture composed of numerous curved and wrinkled nanosheets. These nanosheets are loosely stacked rather than densely packed, suggesting the formation of an open layered framework after thermal treatment. The TEM image further confirms the sheet-like morphology of $CoSn/C_2N$, in which the nanosheets show transparent contrast, folded edges, and overlapping regions, indicating their ultrathin nature and flexible structural characteristics (Fig. 1(c)). The preservation of this wrinkled nanosheet morphology suggests that the supramolecular precursor can effectively direct the formation of a two-dimensional carbon-based framework during pyrolysis. Elemental mapping images reveal that C, N, and the metal elements are uniformly distributed throughout the nanosheet architecture, confirming the successful incorporation of Co and Sn species into the nitrogen-doped carbon matrix (Fig. 1(d)). No large metal aggregates can be observed from the elemental distribution, suggesting that the CoSn species are well dispersed within the carbon framework. The high-resolution STEM images further show numerous bright contrast domains distributed on the nanosheets, which can be assigned to CoSn nanoparticles or nanoclusters anchored on the carbon support (Figs.1(e) and 1(f)). These particles are highly dispersed and closely associated with the surrounding carbon matrix, indicating that the nitrogen-rich framework derived from the precursor can effectively stabilize the CoSn species during high-temperature pyrolysis. The particle size distribution was obtained based on the statistical analysis of the bright CoSn particles observed in HAADF-STEM images. As shown in Fig. 1(g), the particle size mainly falls in the range of approximately 1.0–1.2 nm, with the dominant distribution centered around 1.0–1.1 nm.

Just Accepted

This result confirms the formation of ultrasmall CoSn particles with a relatively narrow size distribution. The small particle size can be associated with the uniform dispersion of metal-containing precursors in the supramolecular intermediate and theanchoring effect of the nitrogen-rich C_2N framework[42-44]. Overall, these structural characterizations demonstrate that $CoSn/C_2N$ possesses a flower-like nanosheet architecture, homogeneous Co/Sn distribution, and highly dispersed ultrasmall CoSn particles supported on the C_2N. The XRD patterns (Fig. S3-S5 in the ESM) show no characteristic diffraction peaks of g-C_3N_4 or large-size metallic/oxide crystals, further supporting the formation of the C_2N framework and the highly dispersed nature of the CoSn species.

Raman spectroscopy was employed to further confirm the nature of the carbon support. As shown in Fig. S6-S8 in the ESM, the Raman spectra of $CoSn/C_2N$, Co/C_2N, and Sn/C_2N all exhibit characteristic D and G bands. The I_D/I_G ratio of $CoSn/C_2N$ was determined to be approximately 0.85, which is consistent with typical values reported for C_2N -based materials. This result, together with elemental analysis (C/N ≈ 2.0) and XRD patterns (Fig. S3-S5), confirms that the support is C_2N rather than g-C_3N_4 or N-doped carbon. High-resolution XPS analysis reveals that the distinct C-N bond in C 1s confirm the formation of the C_2N framework, while the well-defined Co-N bond in N 1s and the binding energy shifts in Co 2p and Sn 3d jointly evidence the Sn-induced charge transfer and asymmetric electronic distribution (Fig. S9 in the ESM).

As shown in Fig. S10 in the ESM, the N_2 adsorption-desorption isotherms of $CoSn/C_2N$, Co/C_2N, and Sn/C_2N exhibit typical Type IV curves with H3 hysteresis loops, confirming the open framework assembled from stacked nanosheets. Notably, $CoSn/C_2N$ shows the highest BET surface area of 225.0 m^2/g and pore volume of 1.08 cm^3/g, and an average pore size of 13.7 nm. These values are significantly higher than those of Co/C2N (190.0 m^2/g, 0.90 cm^3/g, 12.8 nm) and Sn/C_2N (165.0 m^2/g, 0.78 cm^3/g, 11.8 nm). indicating that the bimetallic CoSn sites and oxalic acid assistance create a highly accessible hierarchical porous structure for efficient catalytic reactions.

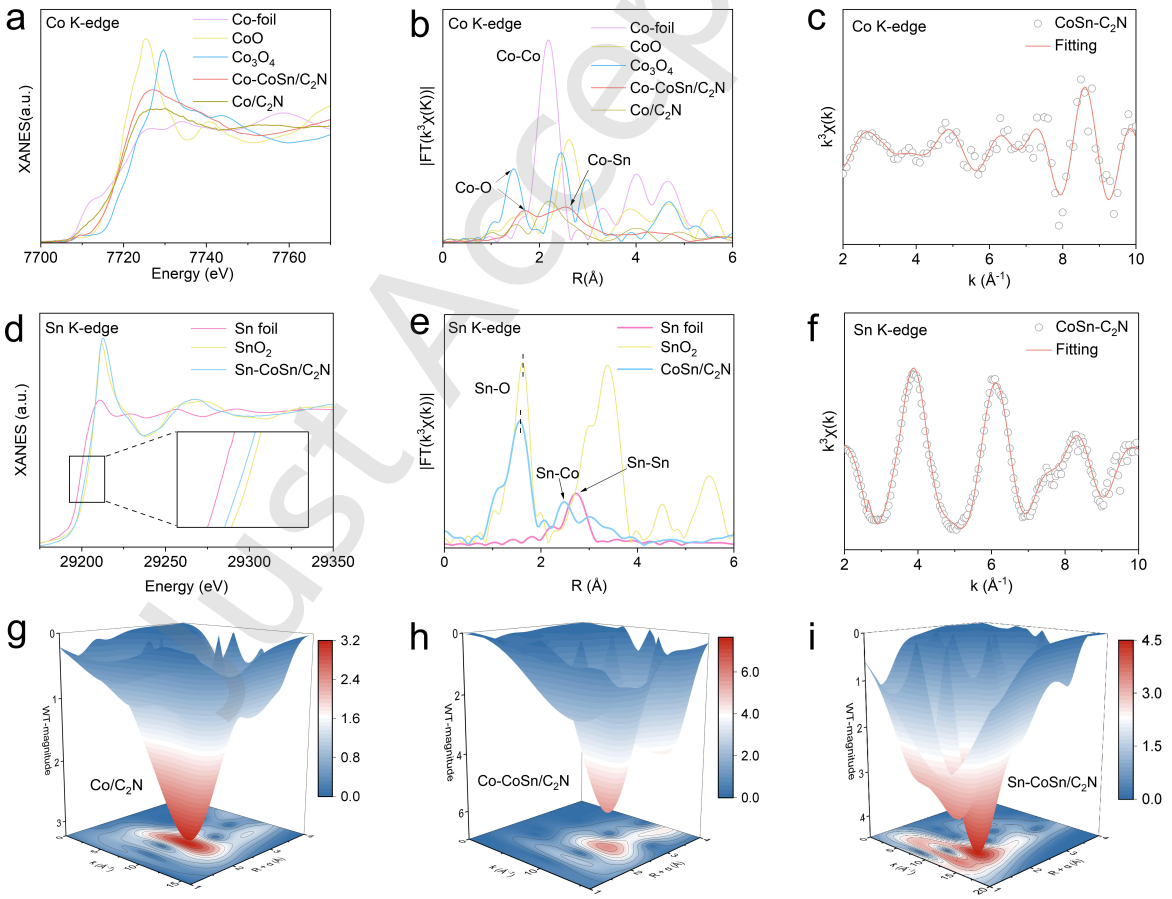


Figure 2 (a) Co K-edge XANES spectra of $CoSn/C_2N$ and reference samples. (b) Co K-edge Fourier-transformed EXAFS spectra of $CoSn/C_2N$ and reference samples. (c) Co K-edge k-space EXAFS fitting curve of $CoSn/C_2N$. (d) Sn K-edge XANES spectra of $CoSn/C_2N$ and reference samples. (e) Sn K-edge Fourier-transformed EXAFS spectra of $CoSn/C_2N$ and reference samples. (f) Sn K-edge k-space EXAFS fitting curve of $CoSn/C_2N$. (g–i) Wavelet-transform EXAFS maps of $CoSn/C_2N$ and related reference samples.

X-ray absorption spectroscopy was employed to further investigate the electronic structure and local coordination environment of $CoSn/C_2N$. As shown in Fig. 2(a), the Co K-edge XANES spectrum of $CoSn/C_2N$ is located between those of Co foil and Co_3O_4, indicating that the Co species in $CoSn/C_2N$ possess a partially oxidized electronic state.

Just Accepted

Regarding the reference samples, Co foil shows a typical metallic pre-edge feature, whereas CoO and Co3O4 exhibit distinct absorption edge shifts toward higher energies corresponding to their +2 and +3 oxidation states, respectively. To more precisely determine the Co oxidation state, first-derivative Co K-edge XANES spectra were analyzed. As shown in Fig. S11 in the ESM, the edge position of $CoSn/C_2N$ is located between those of CoO and Co_3O_4, confirming a mixed valence state of approximately +2.32, which is consistent with the XANES analysis and the Co 2p XPS results. Compared with Co/C_2N, $CoSn/C_2N$ displays an obvious change in the near-edge spectral feature, suggesting that the introduction of Sn modifies the electronic structure around Co sites. The Fourier-transformed Co K-edge EXAFS spectra further reveal the coordination features of Co species (Fig. 2(b)). Co foil exhibits a dominant Co–Co scattering peak, while Co_3O_4 shows characteristic Co–O and higher-shell Co-related scattering peaks. Additionally, the CoO reference displays a prominent Co–O scattering peak at a shorter radial distance compared to Co3O4, offering a clear baseline for comparison. (Fig. S12-S14 in the ESM) In contrast, $CoSn/C_2N$ shows a relatively weakened metal–metal scattering contribution and a distinct coordination feature different from those of Co foil, Co_3O_4, and Co/C_2N. The appearance of the scattering contribution assigned to Co–Sn coordination suggests the formation of bimetallic CoSn particles on the C_2N support. The EXAFS fitting curve agrees well with the experimental data, further confirming the rational local coordination environment around Co in $CoSn/C_2N$ (Fig. 2(c) and Fig. S15-S16 in the ESM). The Sn K-edge XAFS spectra were also analyzed to clarify the chemical state and coordination structure of Sn in $CoSn/C_2N$. As shown in Fig. 2(d), the absorption edge of Sn-$CoSn/C_2N$ is shifted to higher energy compared with Sn foil and is closer to that of SnO_2, indicating that Sn species are in an electron-deficient state[45-46]. In the Sn K-edge Fourier-transformed EXAFS spectra, SnO_2 shows a strong Sn–O scattering peak and pronounced high-shell scattering, whereas Sn foil presents typical Sn–Sn coordination features (Fig. 2(e) and Fig. S17-S19 in the ESM).

The fitting of the Sn K-edge EXAFS spectrum further verifies the local structure around Sn in $CoSn/C_2N$[47]. As shown in Fig. 2(f) and Fig. S20-S21 in the ESM, the fitted curve matches well with the experimental oscillation, demonstrating the reliability of the proposed Sn coordination configuration. The coexistence of Sn–O and Sn–Co coordination suggests that Sn species are partially oxidized and structurally coupled with Co species in the bimetallic particles. Such a local structure is consistent with the XANES results, in which both Co and Sn show non-metallic electronic characteristics due to their interaction with the surrounding C_2N framework and neighboring metal atoms. Wavelet-transform EXAFS analysis was further used to distinguish the backscattering atoms and provide complementary information in both R and k spaces. As shown in Figs. 2(g)–2(i), Co/C_2N and $CoSn/C_2N$ display different WT intensity distributions at the Co K-edge, indicating that the coordination environment of Co is significantly changed after the introduction of Sn. The WT maximum of $CoSn/C_2N$ appears in a region different from that of Co/C_2N, further supporting the presence of Co–Sn coordination. In addition, the Sn K-edge WT contour plot of $CoSn/C_2N$ exhibits characteristic intensity maxima associated with Sn-related metal coordination, which is distinguishable from the features of simple Sn–O coordination. These WT results provide additional evidence for the formation of CoSn bimetallic particles on the C_2N support. Overall, the combined XANES, EXAFS fitting, and WT-EXAFS analyses demonstrate that Co and Sn are successfully integrated into the C_2N framework to form ultrasmall CoSn particles. The species are highly dispersed as small clusters on the C_2N support, rather than existing as bulk metal or oxide crystals. The coexistence of Co–Sn, Sn–Co, and metal–support coordination features confirm the formation of a distinct $CoSn/C_2N$ structure with intimate interaction between the bimetallic particles and the nitrogen-rich carbon framework. (Table S1 and S2 in the ESM). These XAFS, XPS, and WT-EXAFS results collectively confirm the three aspects of asymmetry: unequal coordination numbers, charge redistribution, and heteronuclear Co–Sn sites.

Just Accepted

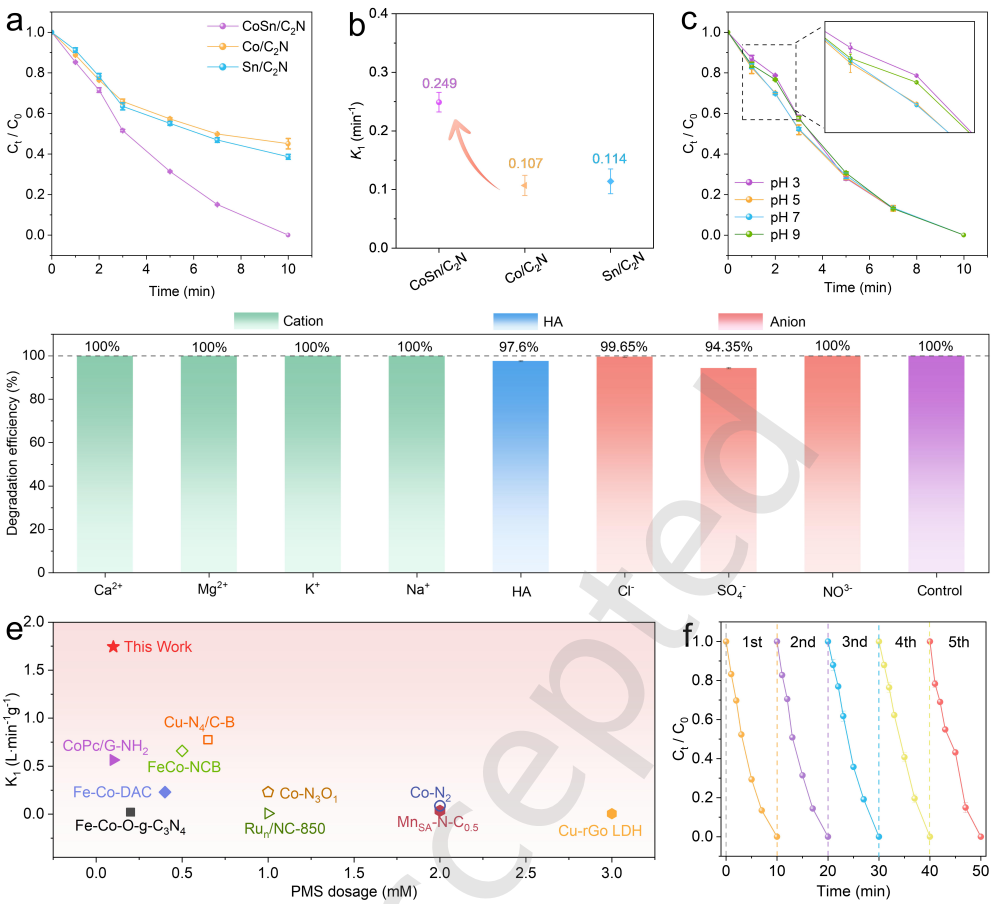


Figure 3 Fenton-like properties of $CoSn/C_2N$. (a) Degradation of SCP in different catalytic systems. (b) The k_1 values of SCP in different catalytic systems. (c) Effect of initial pH. (d) Effects of adding anions, cations and HA to $CoSn/C_2N$/PMS system on SCP degradation within 10 min.(e) Comparison of pollutant removal efficiencies of $CoSn/C_2N$ with other recently reported catalysts versus PMS dosage. (f) Recycling performance of the $CoSn/C_2N$/PMS system for SCP degradation over five consecutive cycles (10 min per cycle, total 50 min). Reaction condition: [catalyst] = 0.1 g/L, [PMS] = 0.1 g/L, [Pollutants] = 20.0 mg/L, [anions and cation] = 1 mM, [HA] = 5 mg/L and initial pH=3.0~9.0±0.2.

2.2Catalytic properties of Fenton-like reactions

Sulfachloropyridazine (SCP) is a typical sulfonamide antibiotic frequently detected in pharmaceutical and livestock wastewater, was selected as the target contaminant to evaluate the catalytic activity of the $CoSn/C_2N$ system toward PMS activation[48]. To exclude the possibility that the enhanced catalytic activity of $CoSn/C_2N$ originates from a higher loading of either Co or Sn rather than a genuine bimetallic synergy, the actual Co and Sn contents were determined by ICP-OES. The results show that $CoSn/C_2N$ contains 11.8 wt% Co and 10.9 wt% Sn, while Co/C_2N contains approximately 12.7 wt% Co and Sn/C_2N contains approximately 12.9 wt% Sn. The Co loading in $CoSn/C_2N$ is comparable to that in Co/C_2N, and the Sn loading is comparable to that in Sn/C_2N, indicating that the superior performance of $CoSn/C_2N$ is not due to a higher content of either individual metal, but rather arises from the synergistic interaction between Co and Sn within the bimetallic system.As shown in Fig. 3(a), $CoSn/C_2N$ exhibited a much faster SCP degradation rate than the monometallic Co/C_2N and Sn/C_2N counterparts under identical reaction conditions. In the $CoSn/C_2N$/PMS system, SCP was completely removed within 10 min, whereas Co/C_2N and Sn/C_2N showed only moderate degradation efficiencies of approximately 54.9% and 61.4%, respectively. The significantly improved degradation efficiency of $CoSn/C_2N$ suggests that the simultaneous incorporation of Co and Sn species into the C_2N framework is essential for promoting PMS activation. Compared with the single-metal systems, the bimetallic CoSn particles supported on C_2N may provide more favorable interfacial electronic interactions and facilitate the activation of PMS, thereby accelerating the oxidative degradation of SCP. To further quantify the catalytic reaction rate, the degradation kinetics were analyzed using the pseudo-first-order kinetic model. As displayed in Fig. 3(b), the apparent rate constant of $CoSn/C_2N$ was calculated to be approximately 0.25 min^{-1}, which was obviously higher than those of Sn/C_2N and Co/C_2N. Specifically, the k value of $CoSn/C_2N$ was about 2.8 times that of Sn/C_2N and 3.4 times that of Co/C_2N, confirming the superior kinetic behavior of the bimetallic catalyst. This result indicates that the enhanced catalytic activity cannot be simply attributed to the individual contribution of Co or Sn species, but is more likely associated with the synergistic effect between Co and Sn within the confined C_2N. The C_2N support with abundant nitrogen sites may also contribute to stabilizing the CoSn particles and modulating their local coordination environment, which is

Just Accepted

beneficial for establishing efficient active interfaces for PMS activation.

The effect of initial solution pH on SCP degradation was then investigated to evaluate the environmental adaptability of the CoSn/C_2N/PMS system. As shown in Fig. 3(c), CoSn/C_2N maintained high SCP degradation efficiency over a wide pH range from acidic to alkaline conditions. SCP could be completely degraded within 10 min at pH 3, 5, 7, and 9, indicating that the catalytic system is not strongly restricted by the initial pH of the solution. Although slight differences in the degradation rate were observed at the early stage of the reaction, the final removal efficiencies remained almost unchanged. This broad pH tolerance is important for practical water treatment, because real wastewater usually presents variable pH conditions depending on its source and composition. To examine the applicability of CoSn/C_2N in complex water matrices, the effects of common inorganic ions and natural organic matter on SCP degradation were further studied. As shown in Fig. 3(d), the presence of Na^+, K^+, Ca^{2+}, Mg^{2+}, NO_3^-, and Cl^- had little influence on the degradation of SCP, and nearly complete removal could still be achieved within 10 min. In comparison, humic acid and SO_4^{2-} caused slight inhibition, with SCP removal efficiencies remaining at approximately 96.4% and 94.3%, respectively. The inhibitory effect of humic acid may be related to the competitive consumption of reactive species or the occupation of active sites on the catalyst surface, while SO_4^{2-} may partially interfere with the oxidation process through interaction with reactive intermediates. Nevertheless, the CoSn/C_2N/PMS system still retained high degradation efficiency in the presence of these interfering substances, demonstrating its good anti-interference capability and potential applicability in complicated aqueous environments.

The catalytic performance of CoSn/C_2N was further compared with previously reported catalysts for sulfonamide antibiotic degradation, as summarized in Fig. 3(e) and Table S3 in the ESM. Compared with these reported PMS-based oxidation systems, CoSn/C_2N exhibited a competitive degradation rate under relatively mild reaction conditions. The high activity of CoSn/C_2N can be attributed to the rational construction of CoSn bimetallic particles on the C_2N support, where the interaction between Co, Sn, and the nitrogen-rich carbon framework may promote electron redistribution and accelerate PMS activation. This comparison highlights the advantage of using C_2N as a confined support to stabilize bimetallic particles and construct efficient catalytic interfaces for antibiotic degradation.

The mineralization degree of SCP by the CoSn/C_2N/PMS system was further evaluated by TOC removal measurements (Fig. S22 in the ESM). The TOC removal efficiency reached 11.04% at 10 min, 21.11% at 30 min, and 34.45% at 60 min. Although the TOC removal is lower than the parent compound degradation efficiency—which is consistent with the selective nature of $^1O_2$-mediated oxidation that preferentially attacks specific functional groups rather than fully mineralizing the entire molecular skeleton—the 34.45% TOC removal at 60 min still demonstrates significant mineralization capability, confirming that a considerable proportion of SCP is converted to CO_2 and H_2O rather than merely transformed into other organic intermediates.

The reusability of CoSn/C_2N was finally evaluated through cyclic degradation experiments. As shown in Fig. 3(f), CoSn/C_2N maintained approximately 98% SCP removal after five consecutive cycles (total reaction time: 50 min), indicating that the catalyst possessed good operational stability during repeated use[49]. Although a slight decrease in the degradation rate was observed after cycling, the final removal efficiency was still maintained, suggesting that the main catalytic structure of CoSn/C_2N was largely preserved. The slight decrease in kinetic rate may be caused by the partial occupation of surface-active sites by reaction intermediates or the inevitable loss of catalyst during the recovery process. To further verify the structural stability, the spent CoSn/C_2N catalyst after cycling was characterized by SEM and XRD. As shown in Fig. S23 and Fig. S24 in the ESM, the catalyst retained its original flower-like nanosheet morphology without obvious particle agglomeration or structural collapse, and the XRD pattern showed no significant changes in the crystal structure, confirming the good structural stability of CoSn/C_2N during the catalytic reaction. To evaluate the metal leaching risk, ICP-OES analysis was performed on the filtrate after the reaction, showing Co leaching below 0.1 mg/L and Sn leaching below 0.05 mg/L. To further confirm whether the leached Co^{2+} ions contribute to SCP degradation, a control experiment was conducted using a $Co(NO_3)_2$ solution with Co^{2+} concentration equivalent to the leached amount, in the absence of the catalyst (Fig. S25 in the ESM). Under the same conditions with PMS addition, almost no SCP degradation was observed, confirming that the leached trace metal ions make a negligible contribution to the catalytic degradation. Overall, these results demonstrate that CoSn/C_2N is an efficient and reusable PMS activation catalyst for SCP degradation, with high catalytic activity, broad pH adaptability, strong resistance to common coexisting substances, and good cycling stability.

Just Accepted

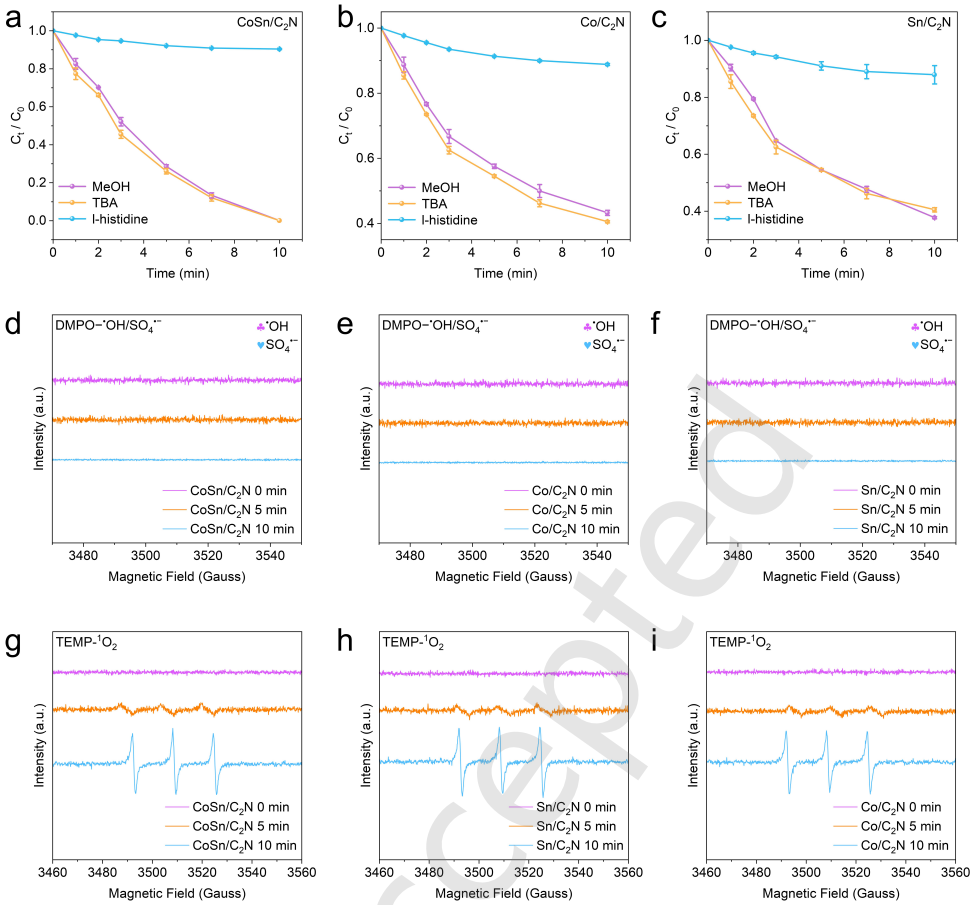


Figure 4 Quenching experiments for SCP degradation with different scavengers, including MeOH, TBA, and L-histidine in the (a) $CoSn/C_2N$/PMS, (b) Co/C_2N/PMS, and (c) Sn/C_2N/PMS systems. EPR spectra recorded with DMPO as the spin-trapping agent for detecting $^{\bullet}OH$ and $SO_4^{\bullet-}$ at 0, 5 and 10 min in the (d) $CoSn/C_2N$/PMS, (e) Co/C_2N/PMS, and (f) Sn/C_2N/PMS systems. EPR spectra recorded with TEMP as the spin-trapping agent for detecting $^1O_2$at 0, 5 and 10 min in the (g) $CoSn/C_2N$/PMS, (h) Sn/C_2N/PMS, and (i) Co/C_2N/PMS systems.

To clarify the reactive oxygen species responsible for SCP degradation, radical quenching experiments and EPRh spin-trapping measurements were carried out for $CoSn/C_2N$, Co/C_2N, and Sn/C_2N systems. Methanol (MeOH) and tert-butanol (TBA) were selected as scavengers for radical species, in which MeOH can quench both $SO_4^{\bullet-}$ and $^{\bullet}OH$, while TBA is generally more sensitive toward $^{\bullet}OH$. As shown in Figs. 4(a)–4(c), the addition of MeOH or TBA caused negligible suppression of SCP degradation in all three systems. For $CoSn/C_2N$, the SCP removal process was almost unchanged after adding MeOH or TBA, suggesting that conventional radical species were not the dominant oxidants. Similar results were also observed for Co/C_2N and Sn/C_2N, where the degradation curves in the presence of MeOH or TBA remained close to those of the corresponding unquenched systems[50,56]. These results indicate that neither $^{\bullet}OH$ nor $SO_4^{\bullet-}$ played a decisive role in SCP oxidation. In contrast, the introduction of L-histidine, a typical quencher for singlet oxygen, significantly inhibited SCP degradation. In the $CoSn/C_2N$/PMS system, SCP removal was strongly suppressed after the addition of L-histidine, and only about 9.6% of SCP was removed within 10 min. Similar inhibition was also observed in the Co/C_2N and Sn/C_2N systems, with final SCP removal efficiencies of approximately 11.2% and 12.1%, respectively. The sharp decrease in degradation efficiency after L-histidine addition demonstrates that $^1O_2$ is the predominant reactive oxygen species in these PMS activation systems. Therefore, the oxidation of SCP over $CoSn/C_2N$, Co/C_2N, and Sn/C_2N is mainly governed by a singlet-oxygen-mediated pathway rather than the conventional sulfate-radical or hydroxyl-radical pathway.

To rule out the involvement of high-valent metal-oxo species in the $CoSn/C_2N$/PMS system, PMSO was employed as a chemical probe, as PMSO can be selectively oxidized to $PMSO_2$ by high-valent metal-oxo species. In the PMS-alone control system, PMSO was slowly oxidized by PMS to $PMSO_2$ (Fig. S26 in the ESM). Notably, as shown in Fig. S27 in the ESM, the consumption rate of PMSO in the $CoSn/C_2N$/PMS system is nearly identical to that in the PMS-alone control system, and the addition of the $CoSn/C_2N$ catalyst does not accelerate the oxidation of PMSO. This result demonstrates that no high-valent metal-oxo species (such as high-valent cobalt-oxo species) are involved in the $CoSn/C_2N$/PMS system, further confirming that SCP degradation proceeds primarily through the non-radical $^1O_2$ pathway.

EPR spectroscopy was further employed to directly verify the generation of reactive oxygen species. DMPO was first used as the spin-trapping agent to detect $^{\bullet}OH$ and $SO_4^{\bullet-}$. As

Just Accepted

shown in Figs. 4(d)–4(f), no obvious DMPO–·OH or DMPO–$SO_4^{\cdot-}$ signals were detected for CoSn/C_2N, Co/C_2N, or Sn/C_2N at 0, 5, and 10 min. The absence of detectable DMPO-radical adduct signals is consistent with the quenching results, further confirming that free radicals are not the major active species under the present reaction conditions. This result also suggests that the PMS activation process over these C_2N-based catalysts does not mainly proceed through a free-radical-dominated route. TEMP was then used as the spin-trapping agent to detect singlet oxygen. As shown in Figs. 4(g)–4(i), no obvious TEMP-related signal was observed at 0 and 5 min, indicating that $^1O_2$ was not generated before the reaction. After 10 min of reaction, distinct characteristic signals assigned to TEMP–$^1O_2$ appeared in the CoSn/C_2N, Sn/C_2N, and Co/C_2N systems. The emergence of these signals provides direct evidence for the formation of $^1O_2$ during PMS activation. Together with the significant inhibition caused by L-histidine, the TEMP-EPR results strongly confirm that $^1O_2$ is the dominant reactive oxygen species responsible for SCP degradation.

Based on the above results, a nonradical oxidation mechanism can be proposed for SCP degradation over CoSn/C_2N. During the reaction, PMS is activated on the surface of the C_2N-supported metal sites, leading primarily to the generation of singlet oxygen rather than ·OH or $SO_4^{\cdot-}$. The nitrogen-rich C_2N framework may provide anchoring sites and interfacial environments for the CoSn particles, while the coexistence of Co and Sn may regulate the local electronic structure of the bimetallic sites. Such structural characteristics are favorable for PMS adsorption and nonradical activation, thereby promoting the formation of $^1O_2$. To quantitatively compare the $^1O_2$ yields among the three catalysts, chemical probe methods were employed. As shown in Fig. S28 in the ESM, the CoSn/C_2N system exhibits the highest $^1O_2$ yield, significantly higher than those of Co/C_2N and Sn/C_2N, confirming that the bimetallic CoSn sites are more effective in promoting the non-radical pathway. Notably, the nearly 100% $^1O_2$ selectivity observed in the CoSn/C_2N PMS system is comparable to that the CoSn/C_2N/PMS system (Fig. S29 in the ESM), where amorphous engineering of the carbon nitride support drives a high-spin Co state that also favors exclusive $^1O_2$ generation. This comparison suggests that the asymmetric coordination environment of Co, whether induced by bimetallic Sn coupling or by amorphization of the support, promoting the non-radical pathway. The quantitative detection of reactive oxygen species was performed using chemical probe methods. As shown in Fig. S30 in the ESM, ABDA was employed as the probe for $^1O_2$ detection via UV-Vis spectroscopy, TPA was used for ·OH detection via fluorescence spectroscopy, and HBA was used for $SO_4^{\cdot-}$ detection via HPLC. Based on these methods, the concentrations of the three reactive species in the CoSn/ C_2N /PMS system were quantitatively determined. Compared with the monometallic Co/C_2N and Sn/C_2N systems, CoSn/C_2N maintains the same dominant $^1O_2$-mediated pathway but may possess a more efficient interfacial activation process due to the interaction between Co, Sn, and the C_2N support. Overall, the combined quenching and EPR results demonstrate that SCP degradation over CoSn/C_2N is mainly driven by a $^1O_2$-dominated nonradical pathway, while ·OH and $SO_4^{\cdot-}$ contribute negligibly to the oxidation process.

To gain atomic-level insight into the interfacial electronic interaction and reaction pathway of PMS activation, DFT calculations were carried out. The differential charge density diagrams (Fig. S31a-b in the ESM) visualize charge redistribution after PMS adsorption on two catalyst models. Obvious charge accumulation (yellow) and charge depletion (blue) can be observed at the interface between PMS molecule and the catalyst surface for both Co/C_2N and CoSn/C_2N, demonstrating interfacial charge transfer during PMS adsorption. Compared with Co/C_2N, the CoSn/C_2N bimetallic site exhibits more pronounced charge rearrangement, indicating stronger electronic coupling between PMS and the asymmetric CoSn active site.

Fig. S31c in the ESM presents the Gibbs free-energy profiles along the PMS activation pathway, including the initial state (I), PMS adsorption (*PMS, II), formation of $*SO_5^{\bullet-}$ intermediate (III), transition state (TS, IV), and generation of $*SO_4^{2-}$ intermediate (V). At the *PMS adsorption step (Stage II), CoSn/C_2N shows a much more negative Gibbs free energy than Co/C_2N, which confirms that the asymmetric CoSn coordination environment greatly thermodynamically favors PMS adsorption. Throughout the whole reaction coordinate, CoSn/C_2N maintains more favorable free-energy values for intermediate adsorption. Although the two catalysts exhibit comparable transition-state energy barriers, the optimized PMS adsorption and intensified interfacial charge transfer over CoSn/C_2N jointly facilitate the PMS-activated non-radical pathway.

To gain deeper insight into the degradation process, the intermediate products of SCP were identified using LC-MS/MS analysis. As shown in Fig. S32 in the ESM and Fig. S32 in the ESM in the Supporting Information, four main intermediates (P1, P2, P3, and P4) were detected, based on which two distinct degradation pathways are proposed. In Pathway I, the dominant reactive species $^1O_2$ attacks the electron-rich sulfonamide N atom, leading to S–N bond cleavage and the formation of P1 (*m/z* 130.0161) and P2 (*m/z* 146.0121). In Pathway II, $^1O_2$ attacks the sulfonyl S=O group, causing rearrangement and SO_2 extrusion to form P3 (*m/z* 221.0593), which subsequently undergoes dehalogenation and oxidation to yield P4 (*m/z* 203.1065). Both pathways ultimately lead to ring-opening reactions and complete mineralization into small organic acids, CO_2, H_2O, and inorganic ions (NO_3^-, SO_4^{2-}, Cl^-). The identified attack sites—sulfonamide N, the electron-rich C and N atoms on the heterocyclic ring, and the sulfonyl group—are perfectly consistent with the electrophilic nature of $^1O_2$. Furthermore, the ECOSAR toxicity assessment reveals that the acute and chronic toxicities of all four intermediates are significantly reduced compared to the parent SCP, confirming that the $^1O_2$-mediated non-radical pathway effectively mitigates the ecological risks associated with antibiotic wastewater.

3 Conclusions

In summary, CoSn/C_2N was successfully prepared through a supramolecular assembly-assisted pyrolysis strategy, in which melamine and cyanuric acid served as nitrogen-rich

Just Accepted

framework precursors, while CoPc and SnPc provided Co and Sn sources for the in situ formation of bimetallic CoSn particles. Structural characterizations confirmed that the obtained catalyst possessed a flower-like nanosheet morphology, homogeneous Co/Sn distribution, and ultrasmall CoSn particles anchored on the C_2N matrix. XANES, EXAFS fitting, and WT-EXAFS analyses further verified that Co and Sn were incorporated into a locally coordinated bimetallic environment rather than existing as bulk metallic or oxide phases. The coexistence of Co–Sn coordination and metal–support interactions indicates the successful construction of a distinct $CoSn/C_2N$ structure. For PMS activation, $CoSn/C_2N$ displayed markedly enhanced SCP degradation compared with Co/C_2N and Sn/C_2N, achieving complete SCP removal within 10 min and a higher apparent kinetic rate constant. The catalyst maintained efficient degradation over a wide pH range and exhibited good resistance to common inorganic ions and humic acid, indicating its applicability in complex aqueous environments. Moreover, $CoSn/C_2N$ retained complete SCP removal after five consecutive cycles, demonstrating good reusability. Mechanistic investigations revealed that MeOH and TBA had negligible effects on SCP degradation, whereas L-histidine strongly inhibited the reaction. Combined with DMPO- and TEMP-based EPR results, these findings confirm that SCP degradation mainly proceeds through a singlet-oxygen-mediated nonradical pathway, while $^{\bullet}OH$ and $SO_4^{\bullet-}$ make limited contributions. Overall, this study highlights the structural advantage of C_2N-supported CoSn bimetallic particles for efficient nonradical PMS activation and provides useful insights into the design of advanced Fenton-like catalysts for antibiotic pollutant removal.

Acknowledgments

This work was financially supported by the National Natural Science Foundation of China (No. 22375019, 22605011), Beijing Institute of Technology Research Fund Program for Young Scholars (No. 3090012221909), University Natural Science Research Project of Anhui Province (No. 2024AH040186) and Application Project of Bengbu University (No. 2024YYX28QD).

Electronic supporting information

Supporting information is available in the online version of this article.

Data availability

Data will be made available on request.

References

[1]Wang, J.; Shu, Z.; Chen, Z.; Su, J.; Liu, C. Iodide ions enhancing sulfamerazine degradation by horseradish peroxidase/H_2O_2: Degradation products, degradation mechanism and toxicity assessment. *J. Clean. Prod.* **2022**, *337*, 130489.

[2]Sun, K.; Chen, M. H.; Qi, X. M.; Hong, D.; Dai, L. Z.; Li, S.-Y.; Lu, Y. C.; Yu, H. Q. Laccase-evoked removal of antibiotics: Reaction kinetics, conversion mechanisms, and ecotoxicity assessment. Crit. *Rev. Environ. Sci. Technol*. **2024**, *54*, 162–183.

[3]Van Boeckel, T. P.; Gandra, S.; Ashok, A.; Caudron, Q.; Grenfell, B. T.; Levin, S. A.; et al. Global antibiotic consumption 2000 to 2010: An analysis of national pharmaceutical sales data. *Lancet Infect. Dis*. **2014**, *14*, 742–750.

[4]VVan Boeckel, T. P.; Brower, C.; Gilbert, M.; Grenfell, B. T.; Levin, S. A.; Robinson, T. P.; et al. Global trends in antimicrobial use in food animals. *Proc. Natl. Acad. Sci. U.S.A*. **2015**, *112*, 5649–5654.

[5]U.S. Food and Drug Administration. Draft Guidance: The Judicious Use of Medically Important Antimicrobial Drugs In Food-Producing Animals. *Fed. Regist*. **2010**, *75*, 37450–37451.

[6]Gelbrand, H.; Miller-Petrie, M.; Pant, S.; Gandra, S.; Levinson, J.; Barter, D.; et al. The State of the World's Antibiotics 2015. *Wound Healing South. Afr*. **2015**, *8*, 30–34.

[7]Rosenblatt-Farrell, N. The landscape of antibiotic resistance. Environ. Health Perspect. 2009, 117, A244–A250.

[8]Wang, S.; Yuan, R.; Chen, H.; Wang, F.; Zhou, B. Anaerobic biodegradation of four sulfanilamide antibiotics: Kinetics, pathways and microbiological studies. *J. Hazard. Mater*. **2021**, *416*, 125840.

[9]Conde-Cid, M.; Fernandez-Calviño, D.; Novoa-Muñoz, J. C.; Arias-Estévez, M.; Díaz-Ravina, M.; Núñez-Delgado, A.; Fernández-Sanjurjo, M. J.; Álvarez-Rodríguez, E. Degradation of sulfadiazine, sulfachloropyridazine and sulfamethazine in aqueous media. *J. Environ. Manage*. **2018**, *228*, 239–248.

[10]Yin, F.; Wang, S.; Zhang, W.; et al. Sulfachloropyridazine (SCP) effects on anaerobic microorganisms and its degradation pathways. *Chem. Eng. J*. **2023**, *466*, 143049.

[11]Scott, G. I.; Porter, D. E.; Norman, R. S.; et al. Antibiotics as CECs: An overview of the hazards posed by antibiotics and antibiotic resistance. *Front. Mar. Sci*. **2016**, *3*, 24.

[12]Tian, K.; Hu, L.; Li, L.; et al. Recent advances in persulfate-based advanced oxidation processes for organic wastewater treatment. *Chin. Chem. Lett*. **2022**, *33*, 4461–4477.

[13]Chen, M. N.; He, Y. J.; Gu, Z. P. Microwave irradiation activated persulfate and hydrogen peroxide for the treatment of mature landfill leachate effluent from a membrane bioreactor. Sep. *Purif. Technol*. **2020**, *250*, 117111.

[14]Zhu, L.; Ai, Z.; Ho, W.; et al. Core-shell Fe-Fe2O3 nanostructures as effective persulfate activator for degradation of methyl orange. *Sep. Purif. Technol*. **2013**, *108*, 159–165.

[15]Ribeiro, A. R.; Nunes, O. C.; Pereira, M. F. R.; et al. An overview on the advanced oxidation processes applied for the treatment of water pollutants defined in the recently launched Directive 2013/39/EU. *Environ. Int*. **2015**, *75*, 33–51.

[16]Yuan, R.; Ramjaun, S. N.; Wang, Z.; et al. Effects of chloride ion on degradation of Acid Orange 7 by sulfate radical-based advanced oxidation process: Implications for formation of chlorinated aromatic compounds. *J. Hazard. Mater*. **2011**, *196*, 173–179.

[17]Huang, Y. F.; Huang, Y. H. Behavioral evidence of the dominant radicals and intermediates involved in bisphenol A degradation using an efficient Co2+/PMS oxidation process. J. *Hazard. Mater*. **2009**, *162*, 1211–1216.

[18]Hodges, B. C.; Cates, E. L.; Kim, J. H. Challenges and prospects of advanced oxidation water treatment processes using catalytic nanomaterials. *Nat. Nanotechnol*. **2018**, 13, 642–650.

[19]Anipsitakis, G. P.; Dionysiou, D. D. Degradation of organic contaminants in water with sulfate radicals generated by the conjunction of peroxymonosulfate with cobalt. *Environ. Sci. Technol*. **2003**, *37*, 4790–4797.

[20]Anipsitakis, G. P.; Dionysiou, D. D. Radical generation by the interaction of transition metals with common oxidants. *Environ. Sci. Technol*. **2004**, *38*, 3705–3712.

[21]Wang, J.; Wang, S. Activation of persulfate (PS) and peroxymonosulfate (PMS) and application for the degradation of emerging contaminants. *Chem. Eng. J*. **2018**, *334*, 1502–1517.

[22]Song, M.; Zhang, P.; Zhang, F.; et al. Converting the redox inactive P-block metal aluminum into active Fenton-like atomically dispersed catalysts to customize singlet oxygen generation. *Nano Today*. **2025**, *61*, 102663.

[23]Zhang, L.-S.; Jiang, X.-H.; Zhong, Z.-A.; Tian, L.; Sun, Q.; Cui, Y.-T.; Lu, X.; Zou, J.-P.; Luo, S.-L. Carbon nitride supported high-loading Fe single-atom catalyst for activation of peroxymonosulfate to generate 1O2 with 100% selectivity. *Angew. Chem. Int. Ed*. **2021**, *60*, 21751–21755.

[24]Xie, L.; Wang, P.; Li, Y.; et al. Pauling-type adsorption of O2 induced electrocatalytic singlet oxygen production on N–CuO for organic pollutants degradation. *Nat. Commun*. **2022**, *13*, 5560.

[25]Zhang, Z. H.; Dong, X. Y.; Du, X. Y.; et al. Copper-catalyzed enantioselective Sonogashira-type oxidative cross-coupling of unactivated C(sp3)–H bonds with alkynes. *Nat. Commun*. **2019**, *10*, 5689.

Just Accepted

[26]Zhen, J.; Sun, J.; Xu, X.; et al. M–N3 configuration on boron nitride boosts singlet oxygen generation via peroxymonosulfate activation for selective oxidation. *Angew. Chem. Int. Ed*. **2024**, *63*, e202402669.
[27]Zhu, K.; Qin, W.; Chen, Y.; Liang, X.; Xin, H.; Huang, Z.; Garces, H. F.; Gan, Y.; Sillanpää, M.; Qiu, R.; et al. Construction of N-Fe-S bridge in atomic iron catalyst for boosting Fenton-like reactions. *Nano Today*. **2024**, *58*, 102462.
[28]Ghogare, A. A.; Greer, A. Using singlet oxygen to synthesize natural products and drugs. Chem. Rev. **2016**, 116, 9994–10034.
[29]Weng, Z.; Lin, Y.; Guo, S.; Zhang, X.; Guo, Q.; Luo, Y.; Ou, X.; Ma, J.; Zhou, Y.; Jiang, J.; et al. Site engineering of covalent organic frameworks for regulating peroxymonosulfate activation to generate singlet oxygen with 100% selectivity. *Angew. Chem. Int. Ed*. **2023**, *62*, e202310934.
[30]Qi, Z.; Mei, X.; Wang, J.; et al. Ligand-pinning induced size modulation of CsPbI3 perovskite quantum dots for red light-emitting diodes. *Adv. Funct. Mater*. **2024**, *34*, 2405679.
[31]Wang, X.; Xiong, Z.; Shi, H.; Wu, Z.; Huang, B.; Zhang, H.; Zhou, P.; Pan, Z.; Liu, W.; Lai, B. Switching the reaction mechanisms and pollutant degradation routes through active center size-dependent Fenton-like catalysis. *Appl. Catal., B*. **2023**, *329*, 122569.
[32]Yu, Y.; Yu, C.; Wu, Z.; Huang, B.; Zhou, P.; Zhang, H.; Liu, W.; Liu, Y.; Xiong, Z.; Lai, B. Switching the primary mechanism from a radical to a nonradical pathway in electrocatalytic ozonation by onsite alternating anode and cathode. *Chem. Eng. J*. **2023**, *457*, 141340.
[33]Yang, L.; Xiong, Z.; Li, J.; Wu, Z.; Zhao, X.; Zhao, C.; Zhou, Y.; Qian, Y.; Lai, B. Iron active sites encapsulated in N-doped graphite for efficiently selective degradation of emerging contaminants via peroxymonosulfate (PMS) activation: Inherent roles of adsorption and electron-transfer dominated nonradical mechanisms. *Chem. Eng. J*. **2022**, *444*, 136623.
[34]Ding, K.; et al. A general synthesis approach for supported bimetallic nanoparticles via surface inorganometallic chemistry. *Science*. **2018**, *362*, 560–564.
[35]Jia, C.; et al. Prediction of C2N-supported double-atom catalysts with individual/integrated descriptors for electrochemical and thermochemical CO2 reduction. *J. Am. Chem. Soc*. **2025**, *147*, 16864–16875.
[36]Mahmood, J.; Lee, E. K.; Jung, M.; et al. Nitrogenated holey two-dimensional structures. *Nat. Commun*. 2015, *6*, 6486.
[37]Guo, J.; Gao, B.; Li, Q.; et al. Size-dependent catalysis in Fenton-like chemistry: From nanoparticles to single atoms. *Adv. Mater*. **2024**, *36*, 2403965.
[38]Yang, L.; Yang, H.; Yin, S.; et al. Fe single-atom catalyst for efficient and rapid Fenton-like degradation of organics and disinfection against bacteria. *Small*. **2022**, *18*, 2104941.
[39]Wang, L.; Guo, Z.; Hou, Y.; et al. Spin-regulated Fe-Cu diatomic catalytic chemistry enables significant minimization of catalyst consumption with high-efficiency Fenton-like activity. *Angew. Chem. Int. Ed*. **2026**, *65*, e25747.
[40]Jin, S.; Tan, W.; Huang, Y.; et al. Remote tuning of single-atom Fe-N5 sites via high-coordination defects for enhanced Fenton-like water decontamination. *Nat. Commun*. **2025**, *16*, 10455.
[41]Gu, H.; Zhong, L.; Shi, G.; et al. Graphdiyne/graphene heterostructure: A universal 2D scaffold anchoring monodispersed transition-metal phthalocyanines for selective and durable CO2 electroreduction. *J. Am. Chem. Soc*. **2021**, *143*, 8679–8688.
[42]Liu, Y.; Zhang, S.; Jiao, C.; et al. Axial phosphate coordination in Co single atoms boosts electrochemical oxygen evolution. *Adv. Sci*. **2023**, *10*, 2206107.
[43]Zhang, Z.; Sun, Z.; Wei, Z.; Chen, Z.; Sun, Q.; Zhan, Z.; Li, X.; Huang, A.; Li, S.; Chen, W.; et al. Rational design of nano and atomically dispersed catalysts for electrocatalytic ammonia synthesis from nitrate. *eChem*. **2025**, *1*, 2.
[44]Zhan, Z.; Wei, Z.; Zhang, Z.; et al. Precisely designing atomically dispersed catalysts for C-N coupling reactions. *Nano Res. Energy*. 2025, *4*, e9120197.
[45]Wang, X.; Zhang, N.; Shang, H.; et al. Precisely designing asymmetrical selenium-based dual-atom sites for efficient oxygen reduction. *Nat. Commun*. **2025**, *16*, 470.
[46]Liu, L.; Lopez-Haro, M.; Lopes, C.; et al. Structural modulation and direct measurement of subnanometric bimetallic PtSn clusters confined in zeolites. *Nat. Catal*. **2020**, *3*, 628–638.
[47]Liu, L. C.; Corma, A. Bimetallic sites for catalysis: From binuclear metal sites to bimetallic nanoclusters and nanoparticles. *Chem. Rev*. **2023**, *123*, 4855–4933.
[48]Yang, Q.; Li, X.; Zheng, J.; et al. Harnessing antibonding orbital occupancy in Co/Ni bimetallic oxides to boost Fenton-like catalysis. *Chem. Eng. J*. **2026**, 178334.
[49]Shu, D. W.; Zhang, X. Q.; Han, B.; et al. Enhanced degradation and recycling of reactive dye wastewater using cobalt loaded MXene catalysts. *npj Clean Water*. 2024, *7*, 88.
[50]Peng, J. B.; Chang, Y.; Xu, L.; et al. Insights into the enhanced removal of sulfamethoxazole via peroxymonosulfate activation catalyzed by bimetallic (Co/Cu) doped graphitic carbon nitride: Reaction kinetics, mechanisms, and pathways. *Chem. Eng. J*. **2024**, *481*, 148735
[51]Yang, X.; Ma, L.; Wang, S.; Hu, X.; Li, B.; Li, W.; Wang, D.; Dai, Z. Electrochemiluminescence-based multiplex immunoassays for multianalyte bioanalysis: Signal encoding strategies and analytical perspectives. Electrochem. Commun. 2026, 186, 108130.
[52]Huanhuan, Z.; Yanping, F.; Shuyan, G.; Wen-Gang, C.; Mingchang, Z.; Zhenglong, L.; Yuhai, D.; Jiarui, Y.; Zechao, Z.; Zhenluo, Y.; et al. Research progress on Ti-based materials for MgH_2 hydrogen storage systems. Composite Functional Materials 2025, 1 (2), 20250201.
[53]Wang, S.; Wang, L.; Zhou, X.; Fang, J.; Deng, C.; Wang, D. Design principles of single-atom catalysts anchored over porous materials for green catalysis and conversion. Nano Res. 2025, 18 (5), 94907137.
[54]Wang, Y.; Ma, F.; Zhang, G.; Zhang, J.; Zhao, H.; Dong, Y.; Wang, D. Precise synthesis of dual atom sites for electrocatalysis. Nano Res. 2024, 17 (11), 9397-9427.
[55]Yuan, H.; Chen, P.; Li, X.; Xu, X.; Qian, W.; Zhang, H.; Wang, Z.; Fu, H.; Wang, D.; He, D. Scalable fiber-skeleton-reinforced graphene-assembled films enabling wash-durable wearable heating. Nano Res. 2026.
[56]Guo, Y.; Liu, Z.; Zhou, D.; Zhang, M.; Zhang, Y.; Li, R.; Liu, S.; Wang, D.; Dai, Z. Competition and synergistic effects of Ru-based single-atom and cluster catalysts in electrocatalytic reactions. Sci. China Mater. 2024, 67 (6), 1706-1720.

Just Accepted

Electronic Supplementary Material

Asymmetric CoSn coordination-induced Fenton-like reaction

Zheng Liu[1], Jinlong Ge[2], Xuhua Li[1], Xiaoxin Li[1], Jiuli Ruan[1], Ruonan Zhao[1], Han Wang[1], Ting Cao[1], Haiyang Lv[1], Yao Zhu[1], Xin Xia[3], Bingbing Huang[3], Qian Bai[3], Xiaolu Ma[3], Rui Yang[3], Zhengbang Zhu[3], Jilin Li[3], Jingqiao Zhang[1,*], Shuai Li[4,5,*], Yan Gao[2,*]

[1] *State Key Laboratory of Environmental Criteria and Risk Assessment, key Laboratory of Eco-industry of Ministry of Ecology and Environment, Chinese Research Academy of Environmental Sciences, Beijing 100012, China*
[2] *Anhui Provincial Engineering Research Center of Silicon-based Materials, Bengbu University, Bengbu 233030, China*
[3] *Energy & Catalysis Center, School of Materials Science and Engineering, Beijing Institute of Technology, Beijing, 100081, China*
[4] *School of Marine Engineering, Xiamen Ocean Vocational College, Xiamen 361012, China*[5] *College of Environmental Science and Engineering, North China Electric Power University, Beijing 102206, China*

Address correspondence to Jingqiao Zhang, zhangjq@craes.org.cn; Shuai Li, lishuai@163.com; Yan Gao, gaoyan@bbc.edu.cn

Supporting information to https://doi.org/10.26599/NR.2026.94909213

Just Accepted

TEXT S1. CHEMICALS

All chemicals and reagents were analytical reagent (AR) or high-performance liquid chromatography (HPLC) grade. Cobalt (II) phthalocyanine ($C_{32}H_{16}CoN_8$), Tin (II) Phthalocyanine ($C_{32}H_{16}N_8Sn$), Melamine ($C_3H_6N_6$), Cyanuric acid ($C_3H_3N_3O_3$), Oxalic acid ($C_2H_2O_4$), Potassium peroxymonosulfate ($KHSO_5$), Sodium thiosulfate ($Na_2S_2O_3$), L-Histidine ($C_6H_9N_3O_2$), Dimethyl sulfoxide (C_2H_6SO) was obtained from Macklin Biochemical Technology Co., Ltd (China). Sulfachloropyridazine sodium ($C_{10}H_8ClN_4NaO_2S$), purchased from Beijing Bailing Wei Technology Co., Ltd (China). Methanol (CH_3OH), 5,5-Dimethyl-1-pyrroline N-oxide ($C_6H_{11}NO$), 2,2,6,6-tetramethylpiperidine (TEMP) were acquired from Shanghai Aladdin Biochemical Technology Co., Ltd (Shanghai, China). Tert-Butanol ($C_4H_{10}O$) was obtained from Tianjin Damao Chemical Reagent Factory. Ethanol (C_2H_6O) was obtained from Tianjin Komeo Chemical Reagent Co., Ltd (China). Hydrochloric acid, Sulfuric acid (H_2SO_4), and Sodium hydroxide (NaOH) were obtained from Tianjin Chemical Reagent Third Factory. Potassium chloride (KCl), Humic acid (HA) was obtained from Tianjin Beichen Fangzheng Reagent Factory.

TEXT S2. CHARACTERIZATION

The surface morphology information of prepared catalysts was observed transmission electron microscopic (FEI Tecnai F20). A spherical aberration corrected high-angle annular dark-field scanning transmission electron microscope (HADDF-STEM) was applied to observe the CoSn particle on the prepared catalyst. The X-ray diffraction (XRD, SHIMADZU XRD-6000) patterns was performed using an X-ray spectrometer equipped with a Cu-Ka radiation in the 2θ range of 10°-80° at a scan rate 5°/min. Raman spectrum was acquired with a Jobin Yvon Raman spectrometer model HR800. X-ray photon spectroscopy (XPS) measurements were taken in an ESCALab220i-XL (Thermo Scientific) using a monochromatic Al KR X-ray source. The X-ray absorption fine structure spectra data (Co K-edge and Sn K-edge) were conducted at BL11B station and BL14W1 station in Shanghai Synchrotron Radiation Facility (SSRF). The XAFS data were measured at room temperature in fluorescence excitation mode using a Lytle detector. The samples were prepared as plates of 10 mm diameter with 1mm thickness with the addition of PVDF powder as a binder.

TEXT S3. SYNTHESIS OF COSN/C_2N

The prepolymers were first prepared by a one-step method .0.5 g of melamine, 0.1 g of oxalic acid, 0.3 g of Cobalt phthalocyanine (CoPC) and 0.3 g Tin Phthalocyanine (SnPC) were dissolved in 40 mL of DMSO solution, and 0.51 g of cyanuric acid was dissolved in 10 mL of DMSO solution, and both solutions were sonicated for 20 min each, after which they were mixed and stirred for 30 min. the resulting liquid, was pumped and filtered using a pumping machine, and the resulting solid was washed with deionized water and ethanol. It was then dried under vacuum at 60 ℃. The resulting solid was collected by grinding. Calcination at 850 ℃ for 8 h in an argon atmosphere at a ramp rate of 1.2 ℃ min^{-1} gave $CoSn/C_2N$.

TEXT S4. SYNTHESIS OF CO/C_2N

Just Accepted

The prepolymers were first prepared by a one-step method .0.5 g of melamine, 0.1 g of oxalic acid and 0.3 g of Cobalt phthalocyanine (CoPC) were dissolved in 40 mL of DMSO solution, and 0.51 g of cyanuric acid was dissolved in 10 mL of DMSO solution, and both solutions were sonicated for 20 min each, after which they were mixed and stirred for 30 min. the resulting liquid, was pumped and filtered using a pumping machine, and the resulting solid was washed with deionized water and ethanol. It was then dried under vacuum at 60 ℃. The resulting solid was collected by grinding. Calcination at 850 ℃ for 8 h in an argon atmosphere at a ramp rate of 1.2 ℃ min^{-1} gave Co/C_2N.

TEXT S5. SYNTHESIS OF SN/C_2N

The prepolymers were first prepared by a one-step method. 0.5 g of melamine, 0.1 g of oxalic acid and 0.3 g Tin Phthalocyanine (SnPC) were dissolved in 40 mL of DMSO solution, and 0.51 g of cyanuric acid was dissolved in 10 mL of DMSO solution, and both solutions were sonicated for 20 min each, after which they were mixed and stirred for 30 min. the resulting liquid, was pumped and filtered using a pumping machine, and the resulting solid was washed with deionized water and ethanol. It was then dried under vacuum at 60 ℃. The resulting solid was collected by grinding. Calcination at 850 ℃ for 8 h in an argon atmosphere at a ramp rate of 1.2 ℃ min^{-1} gave Sn/C_2N.

TEXT S6. XAFS DATA PROCESSING

The acquired EXAFS data were processed according to the standard procedures using the Athena and Artemis implemented in the IFEFFIT software packages. The fitting detail is described below: The acquired EXAFS data were processed according to the standard procedures using the ATHENA module implemented in the IFEFFIT software packages. The EXAFS spectra were obtained by subtracting the post-edge background from the overall absorption and then normalizing with respect to the edge-jump step. Subsequently, the χ(k) data of Fourier transformed to real (R) space using a hanning window (dk=1.0 $Å^{-1}$) to separate the EXAFS contributions from different coordination shells. To obtain the quantitative structural parameters around central atoms, least-squares curve parameter fitting was performed using the ARTEMIS module of the IFEFFIT software packages. The following EXAFS equation was used:

$$\chi(k)=\sum_j \frac{N_j S_o^2 F_j(k)}{k R_j^2}\exp[-2k^2\sigma_j^2]\exp[\frac{-2R_j}{\lambda(k)}]\sin[2kR_j+\phi_j(k)]$$

S_0^2 is the amplitude reduction factor, $F_j(k)$ is the effective curved-wave backscattering amplitude, Nj is the number of neighbors in the j^{th} atomic shell, R_j is the distance between the X-ray absorbing central atom and the atoms in the j^{th} atomic shell (backscatterer), λ is the mean free path in Å, $\phi_j(k)$ is the phase shift (including the phase shift for each shell and the total central atom phase shift), σ_j is the DebyeWaller parameter of the j^{th} atomic shell (variation of distances around the average R_j). The functions $F_j(k)$, λ, and $\phi_j(k)$ were calculated with the ab initio code FEFF8.2. The additional details for EXAFS simulations are given below. The coordination numbers of model samples (Co foil and Sn foil) were fixed as the

Just Accepted

nominal values. The obtained S_0^2 was fixed in the subsequent fitting of atomically dispersed Co and Sn samples. While the internal atomic distances R, Debye-Waller factor σ^2, and the edge-energy shift ΔE_0 were allowed to run freely.

TEXT S7. CATALYTIC ACTIVITY EVALUATION

1. Experimental methods for the degradation of SCP by the Catalytic.

Take 100 ml of ultrapure water in a 250 mL beaker, so there is no need for adsorption-resolution equilibrium, add 0.01 g PMS to the beaker, stir well, then use NaOH and H_2SO_4 to adjust the solution of the pH = 7, add 1mL of SCP reserve solution, and take several 1.5 mL liquid-phase vials to be used to take the samples. 100 μL of $Na_2S_2O_3$ (100 mM) was added to the vials for depletion of PMS in the sample and left to mix well, 1ml of sample was taken from the beaker and filtered using 0.22 μm filter membrane and put into the vials. Then, 10 mg catalyst was added to start the timing, and the sample was taken using the same method at a fixed time point (1 min, 2 min, 3 min, 5 min, 7 min,10 min). SCP in the filtrate was determined by high-performance liquid chromatography (HPLC) (1260 Infinity II, Agilent, USA).

2. Experimental method for free radical quenching in Catalytic/PMS system:

The quencher was added prior to the addition of SCP using the method described above, and the rest of the steps remained unchanged

3. Catalytic/PMS degradation of SCP with anionic and cationic interference assays:

Add anions and cations before adjusting the pH of the solution by the above method, the rest of the steps remain unchanged.

4. Cyclic degradation experiment:

After one SCP degradation cycle, the catalyst was collected using a 0.22 μm PTFE membrane and dried at 60 ℃. And the obtained powder was reused for the next degradation experiment under the same experimental conditions.

TEXT S8. METHODS OF ANALYZING CONTAMINANTS

An HPLC system consisting of an Agilent Venusil MP C18 column (4.6 mm, 5 μm) was used for the determination of SCP concentration. The mobile phase consisted of methanol and ultrapure water with the volume ratio of 40:60, the flow rate of 1 mL/min, the injection volume of 10 μL, the temperature of the column temperature box at 30 °C, and the detection wavelength of SCP at 270 nm.

Text S9. The calculation of removal efficiency and reaction rate constant

The degradation efficiency of SCP was calculated by the equation:

$$\text{Removal efficiency (\%)} = (C_0 - C_t) / C_0 \times 100\ \%$$

The pseudo-first-order kinetics model:

$$k_1 = -\ln(C_t/C_0)$$

Just Accepted

where C_0 and C_t represent the initial concentration of the pollutant and the concentration at a given reaction time t, respectively. k_1 (min^{-1}) is the reaction rate constant.

Just Accepted

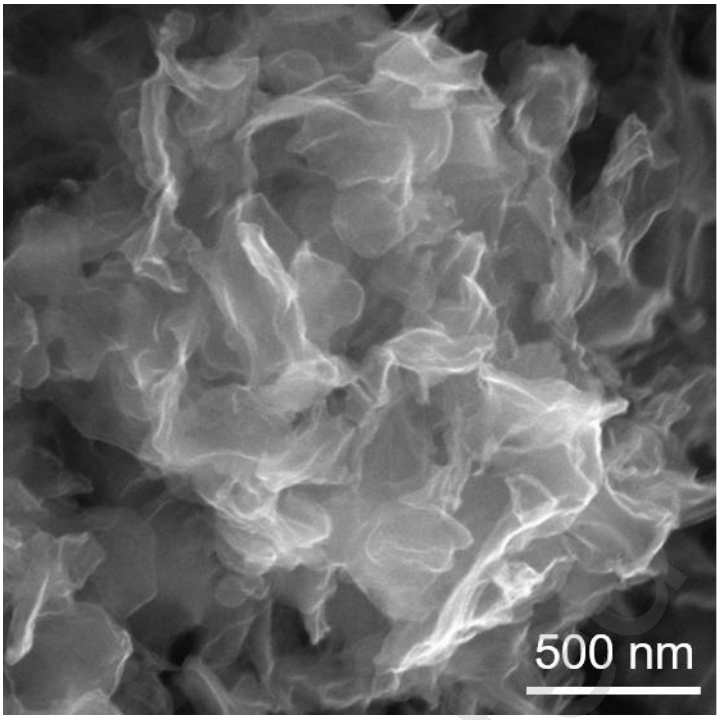


Figure S1. The SEM image of Sn/C_2N.

Just Accepted

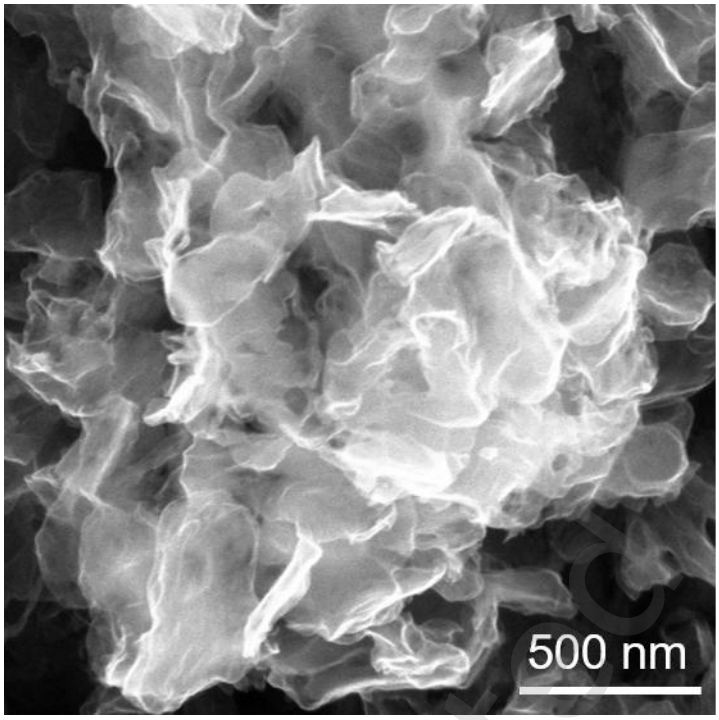


Figure S2. The SEM image of Co/C_2N.

Just Accepted

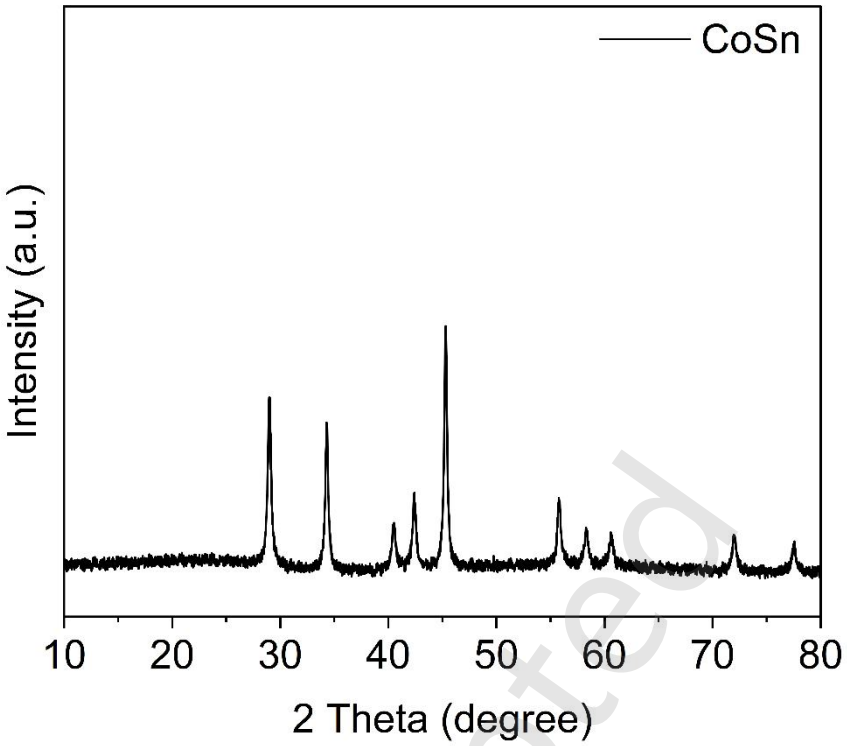


Figure S3. The XRD patterns of $CoSn/C_2N$.

Just Accepted

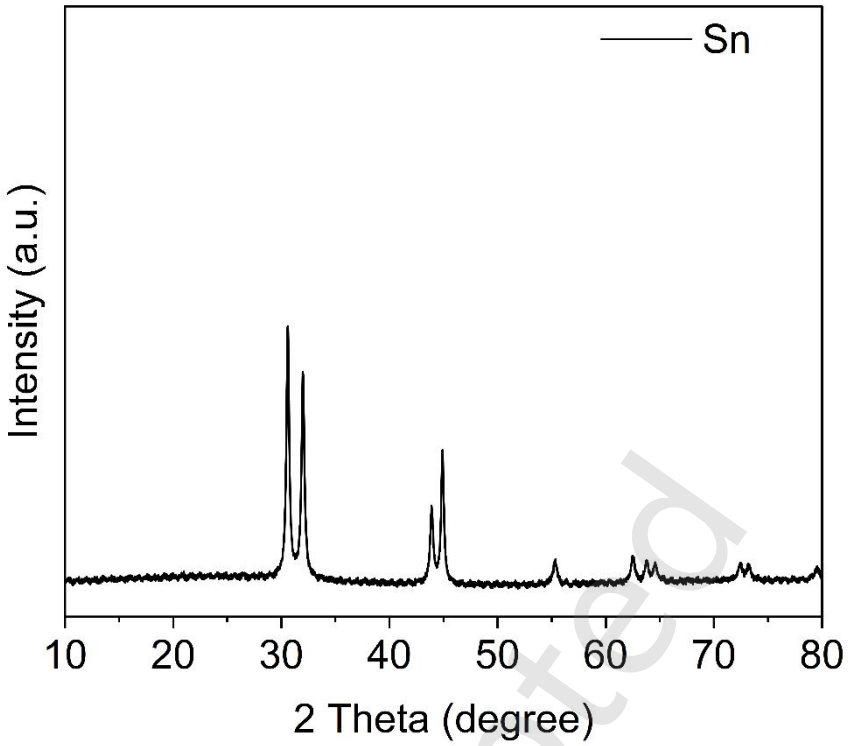


Figure S4. The XRD patterns of Sn/C_2N.

Just Accepted

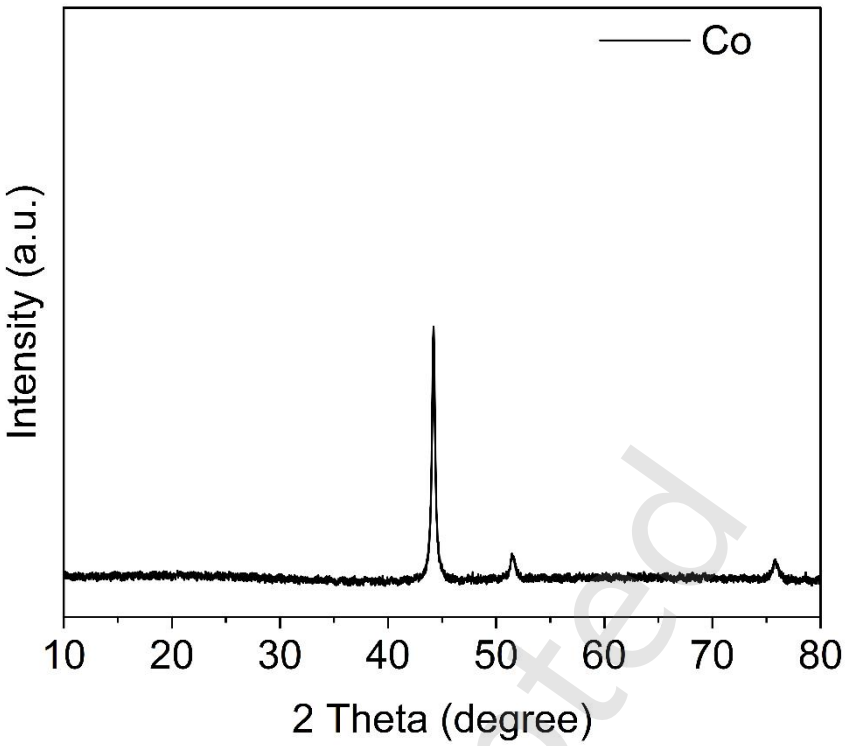


Figure S5. The XRD patterns of Co/C_2N.

Just Accepted

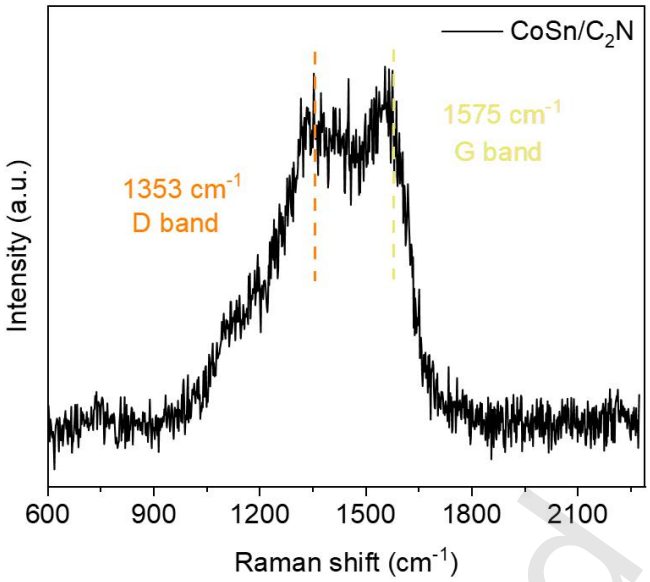


Figure S6. Raman spectra of $CoSn/C_2N$.

Just Accepted

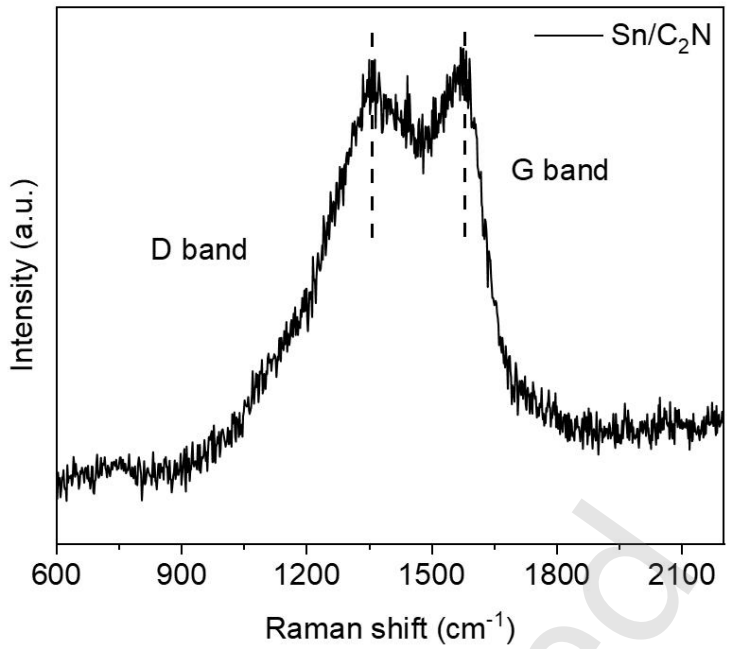


Figure S7 Raman spectra of Sn/C_2N.

Just Accepted

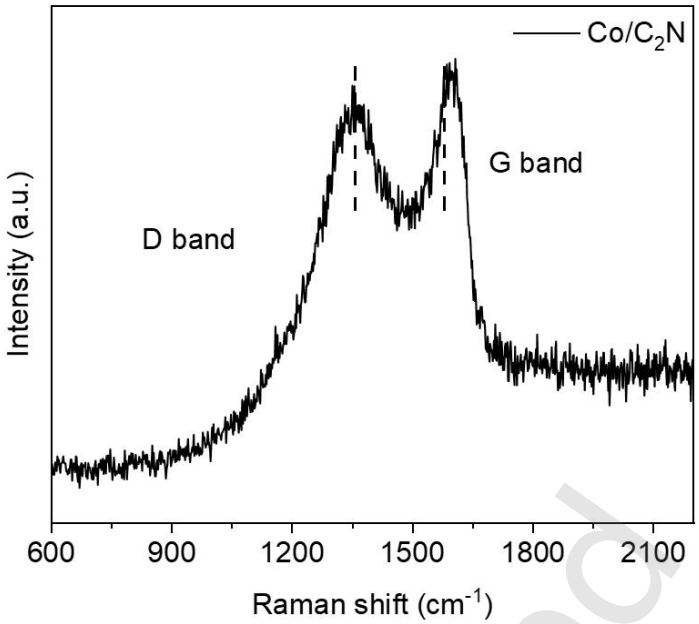


Figure S8 Raman spectra of Co/C_2N.

Just Accepted

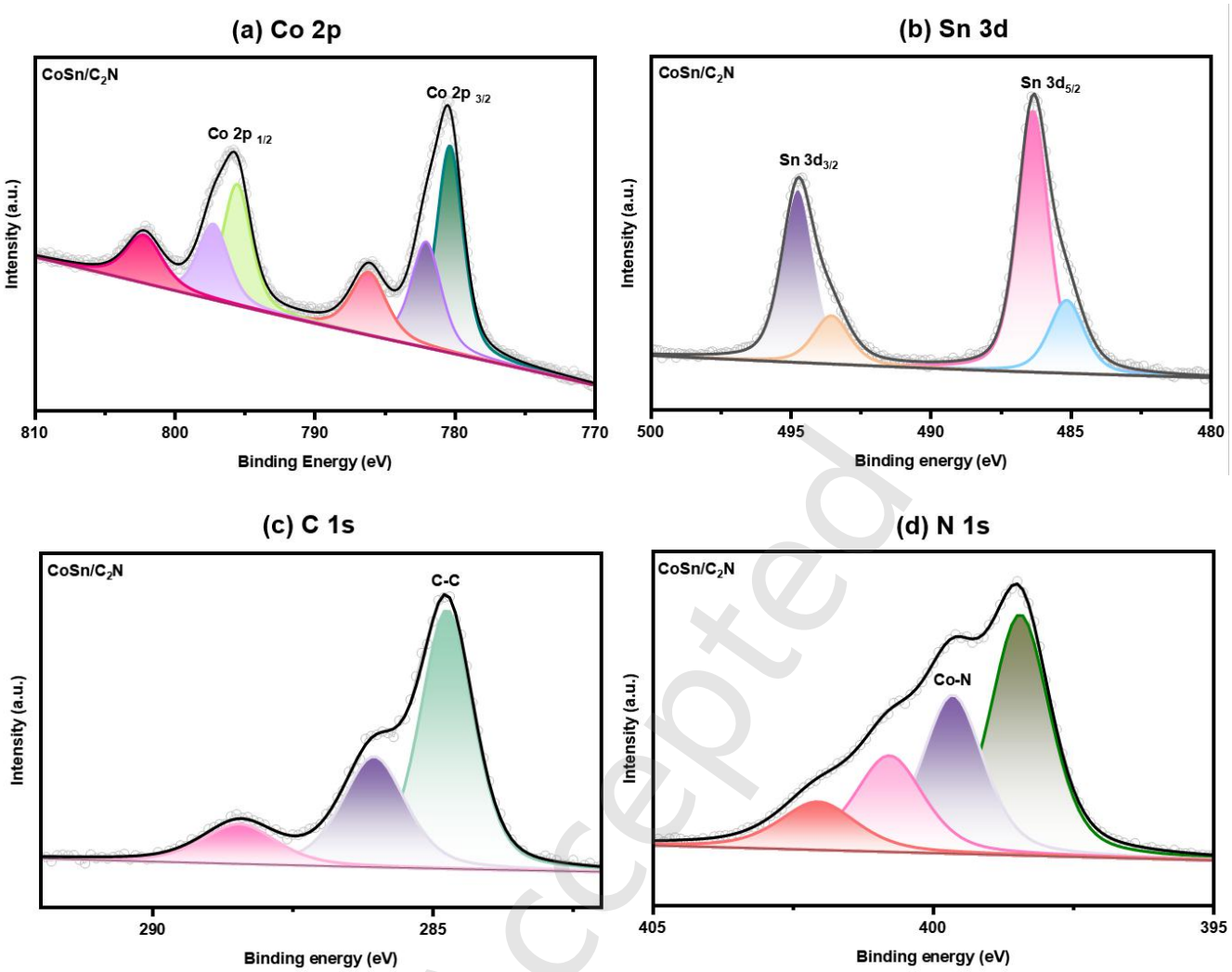


Figure S9. Peak assignments based on typical binding energies of Co, Sn, C and N species in $CoSn/C_2N$ materials.

Just Accepted

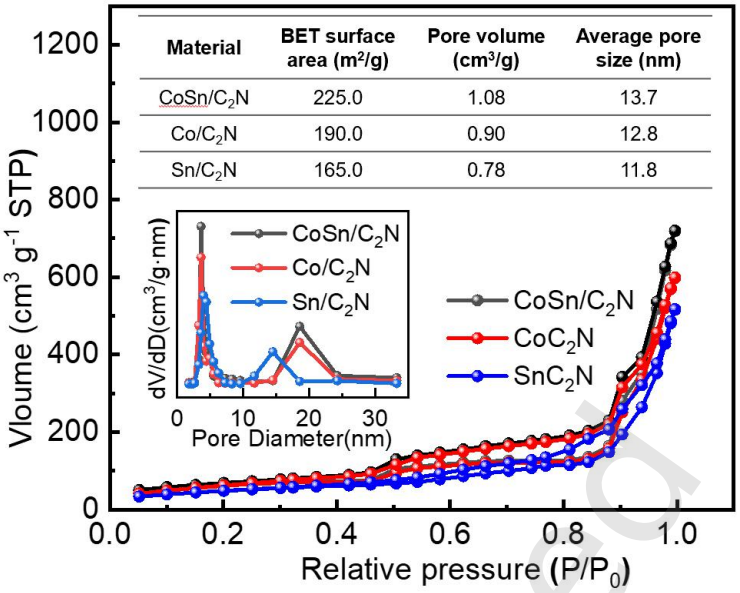


Figure S10. N_2 adsorption/desorption isotherms and pore-size distribution of $CoSn/C_2N$, Co/C_2N and Sn/C_2N.

Just Accepted

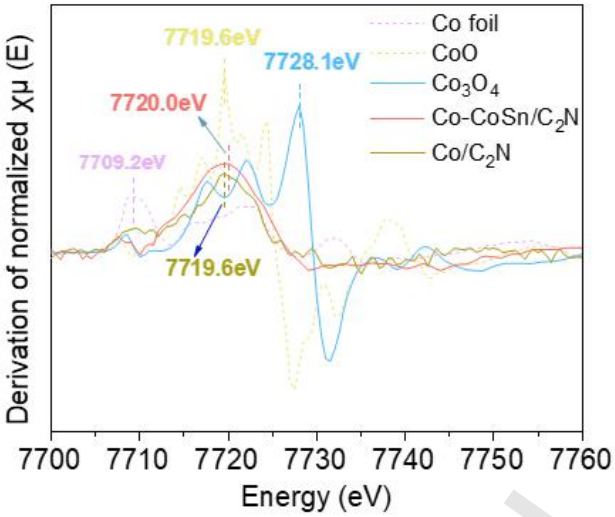


Figure S11. First-derivative Co K-edge XANES spectra of reference samples (Co foil, CoO, Co_3O_4), Co/C_2N and $CoSn/C_2N$.

Just Accepted

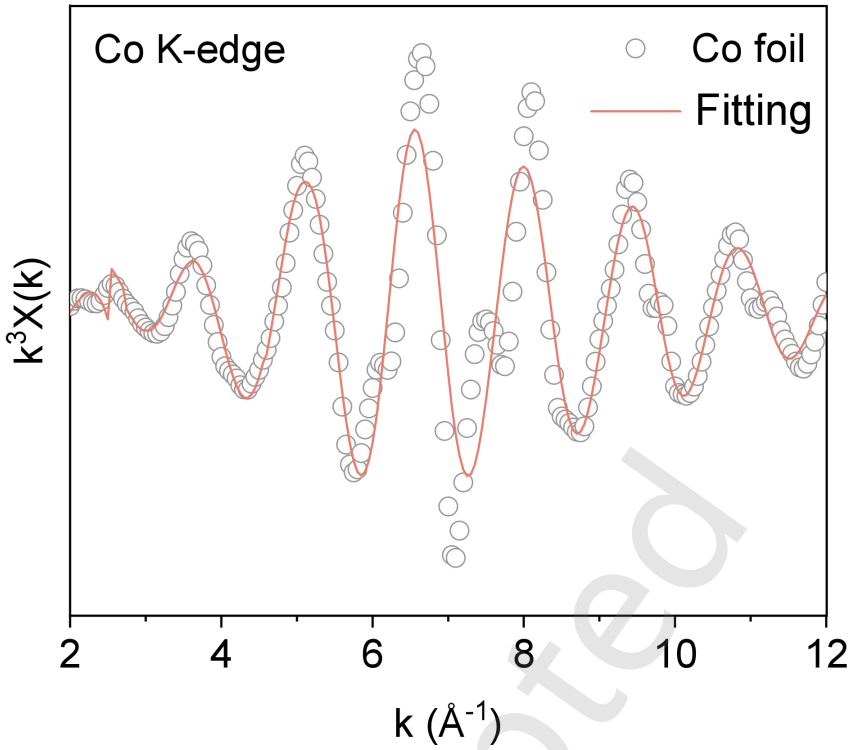


Figure S12. k space FT-EXAFS fitting curves of Co foil.

Just Accepted

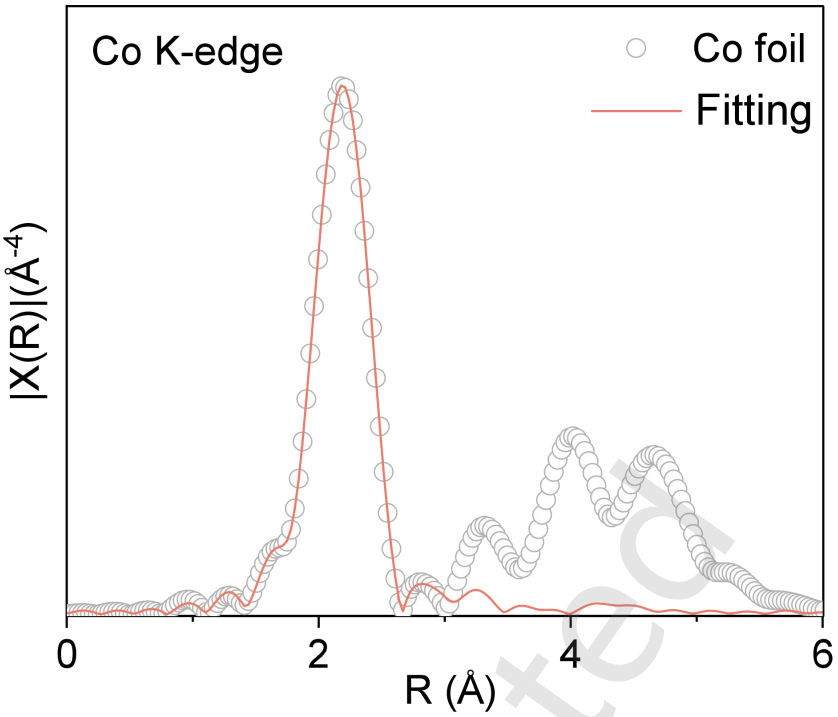


Figure S13. R space FT-EXAFS fitting curves of Co foil.

Just Accepted

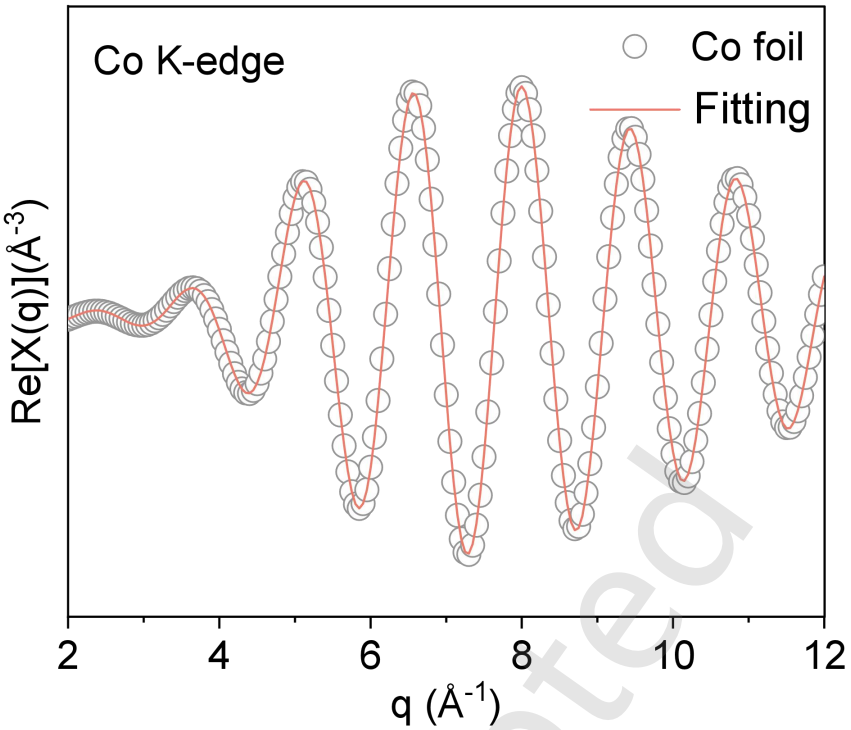


Figure S14. Q space FT-EXAFS fitting curves of Co foil.

Just Accepted

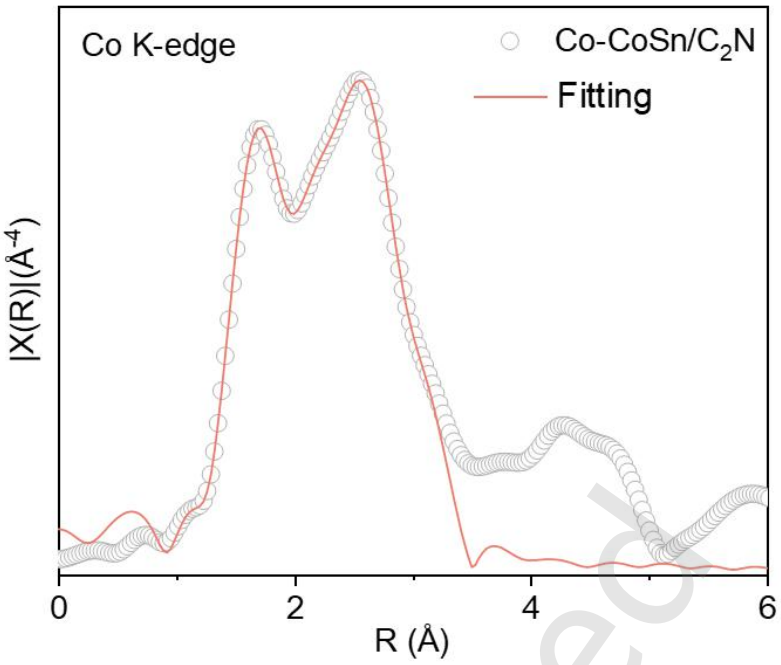


Figure S15. R space FT-EXAFS fitting curves of $CoSn/C_2N$ at Co K-edge.

Just Accepted

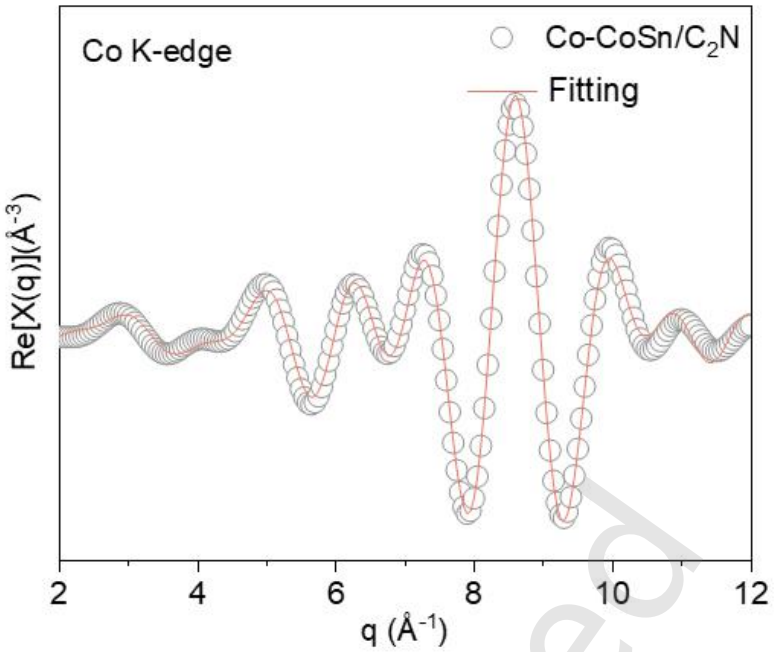


Figure S16. Q space FT-EXAFS fitting curves of $CoSn/C_2N$ at Co K-edge.

Just Accepted

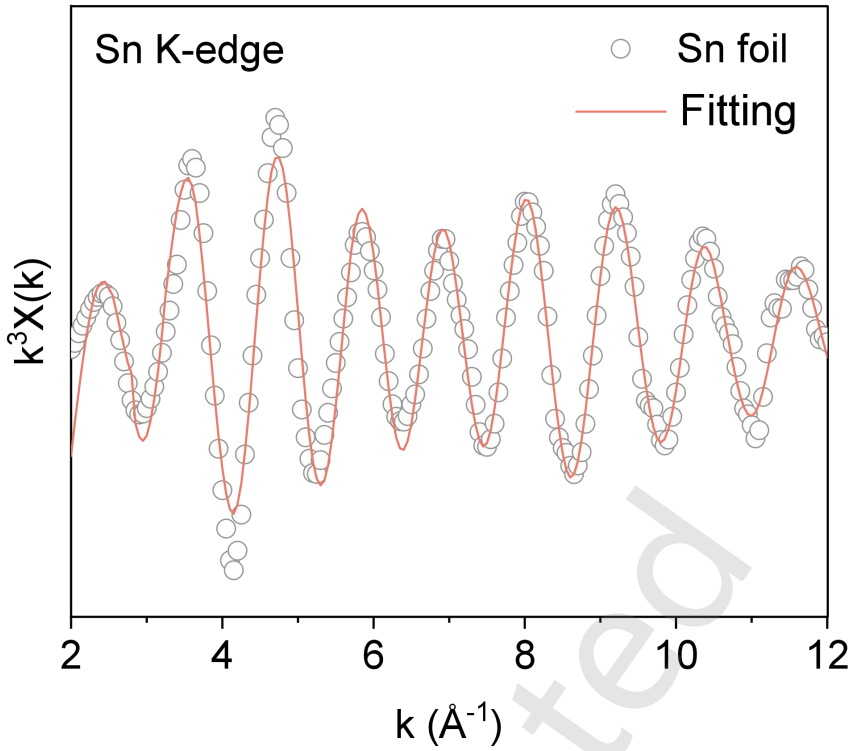


Figure S17. k space FT-EXAFS fitting curves of Sn foil.

Just Accepted

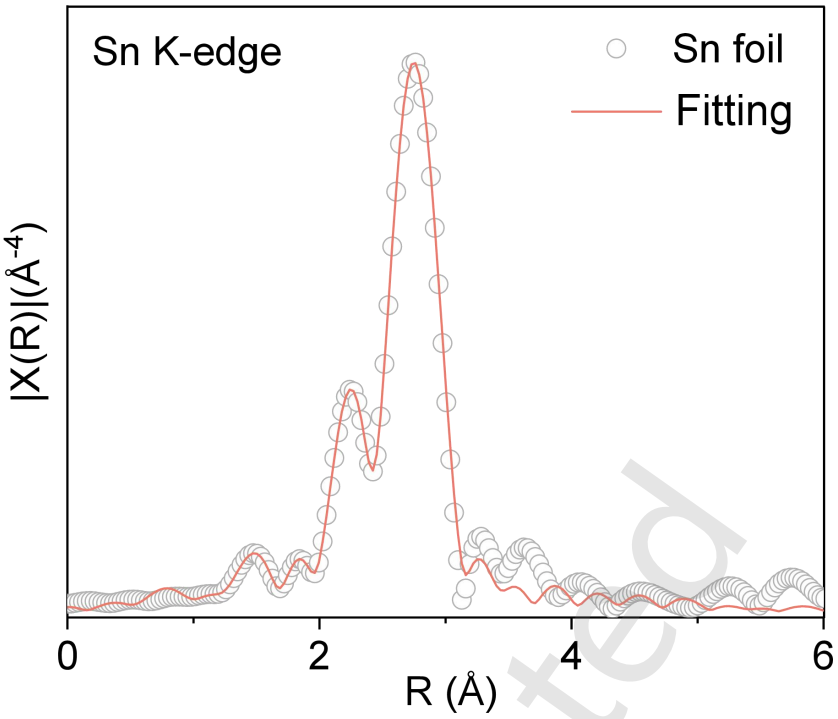


Figure S18. R space FT-EXAFS fitting curves of Sn foil.

Just Accepted

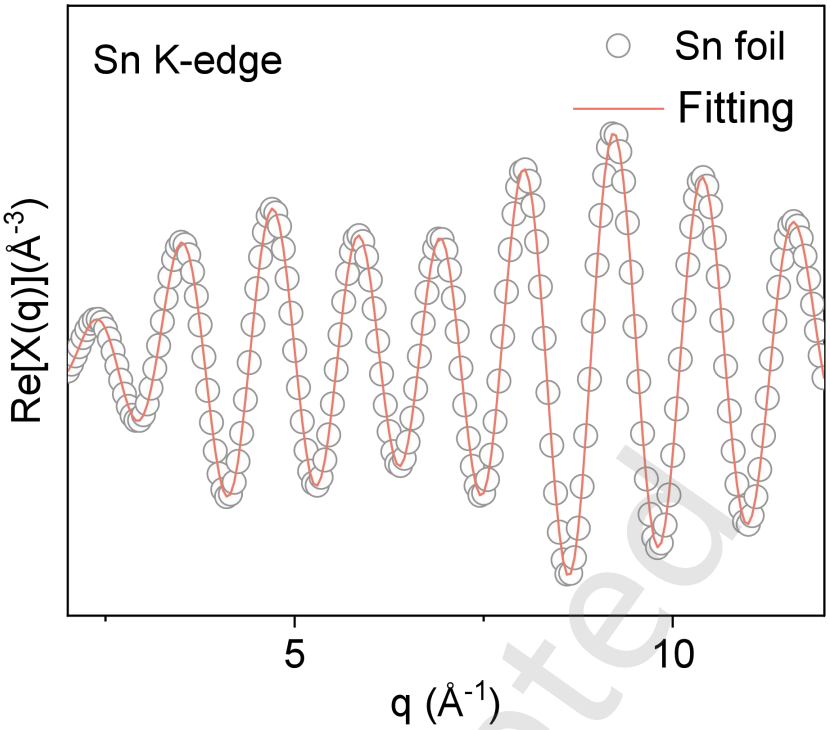


Figure S19. Q space FT-EXAFS fitting curves of Sn foil.

Just Accepted

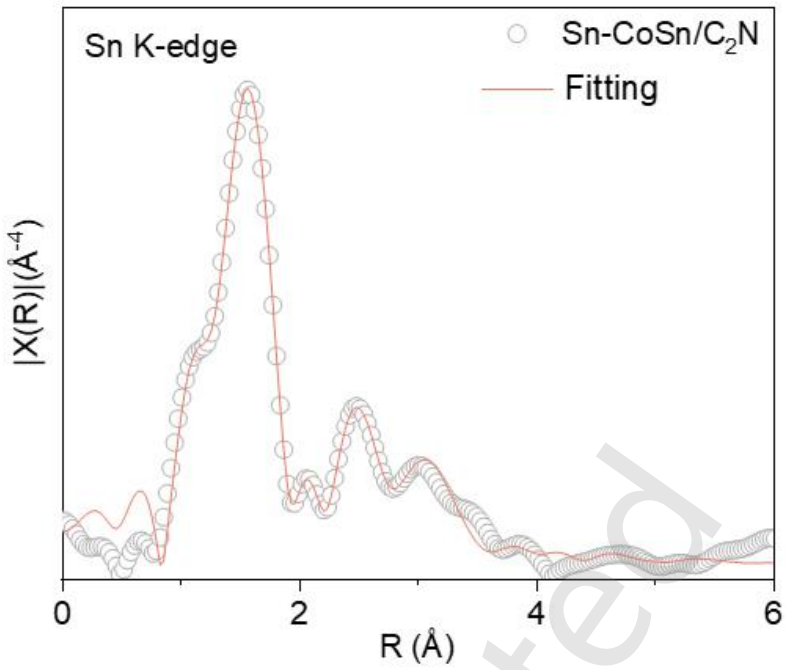


Figure S20. R space FT-EXAFS fitting curves of $CoSn/C_2N$ at Sn K-edge.

Just Accepted

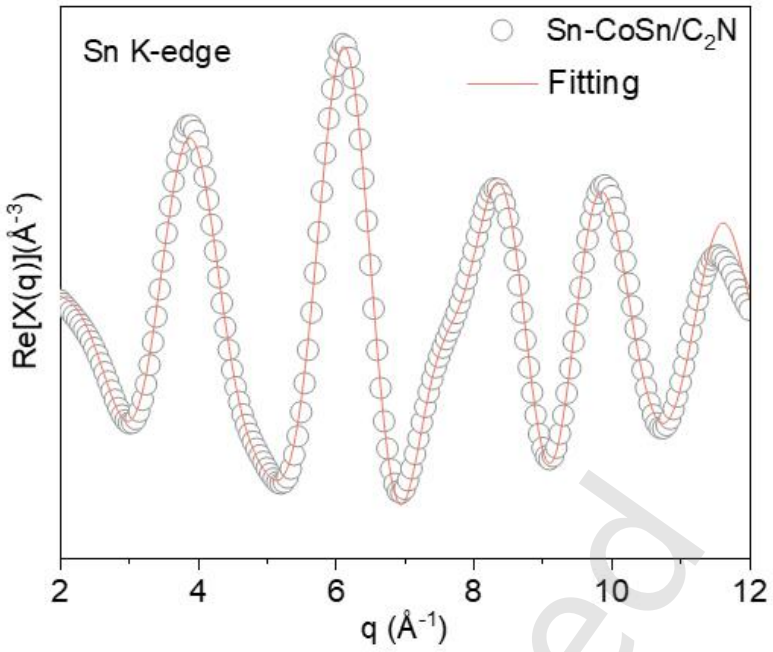


Figure S21. Q space FT-EXAFS fitting curves of $CoSn/C_2N$ at Sn K-edge.

Just Accepted

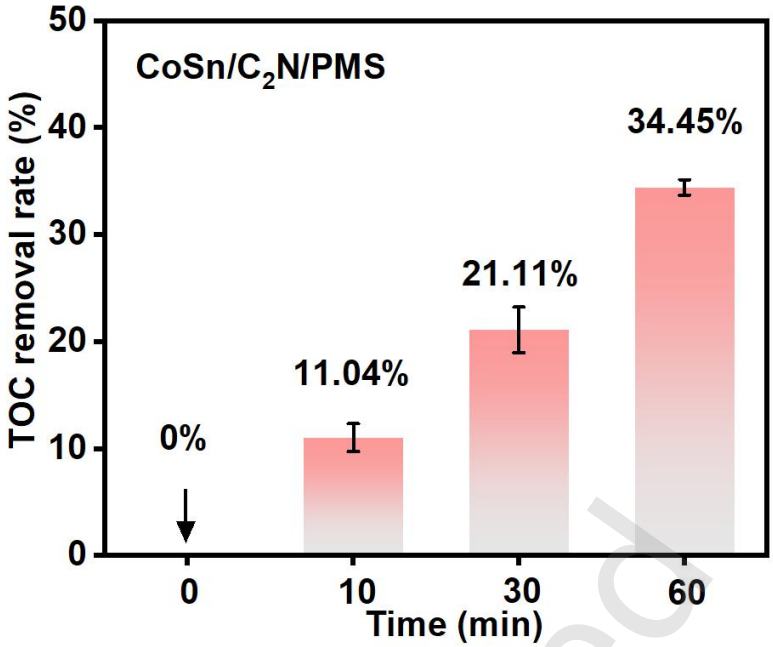


Figure S22. TOC removal rate during SCP degradation in the $CoSn/C_2N$/PMS system.

Just Accepted

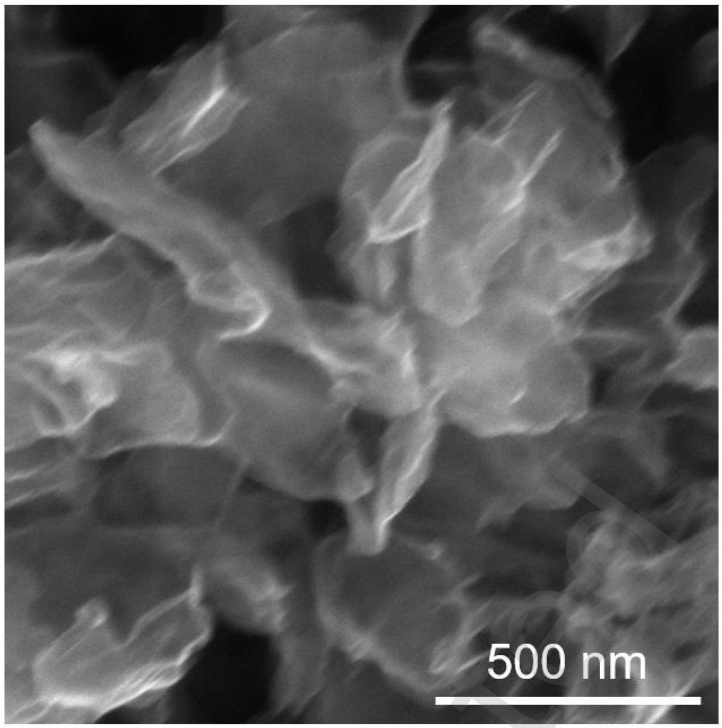


Figure S23. The SEM image of $CoSn/C_2N$ after reaction.

Just Accepted

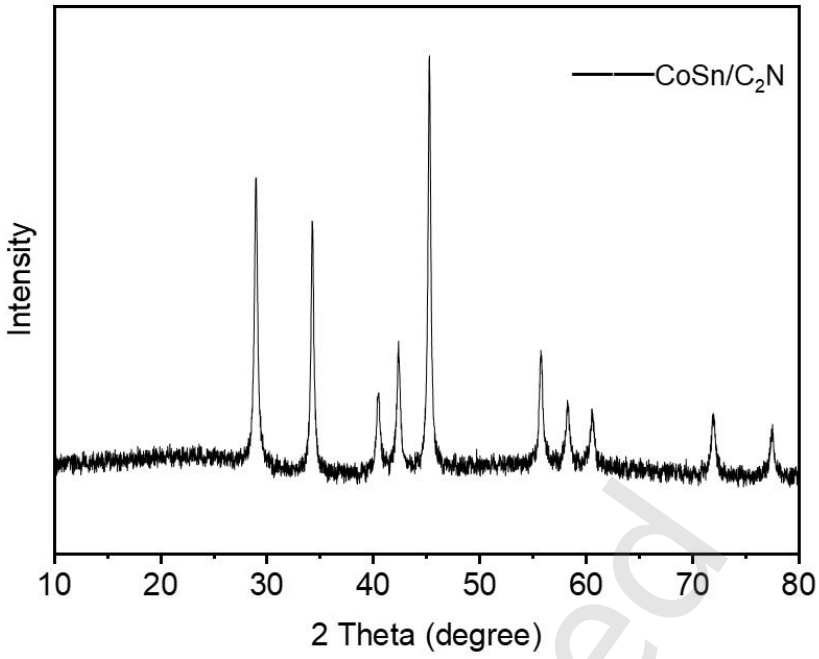


Figure S24. The XRD patterns of $CoSn/C_2N$ after reaction.

Just Accepted

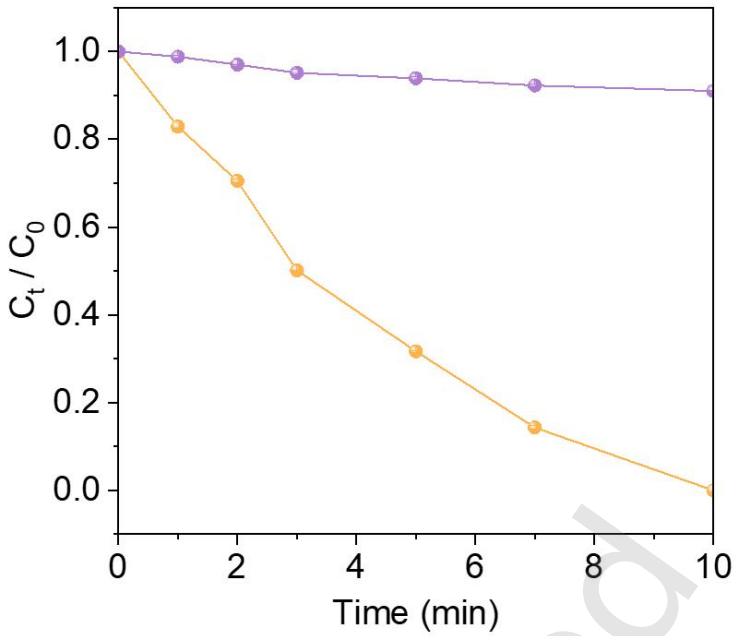


Fig. S25. Dissolution experiment of Co ion.

Just Accepted

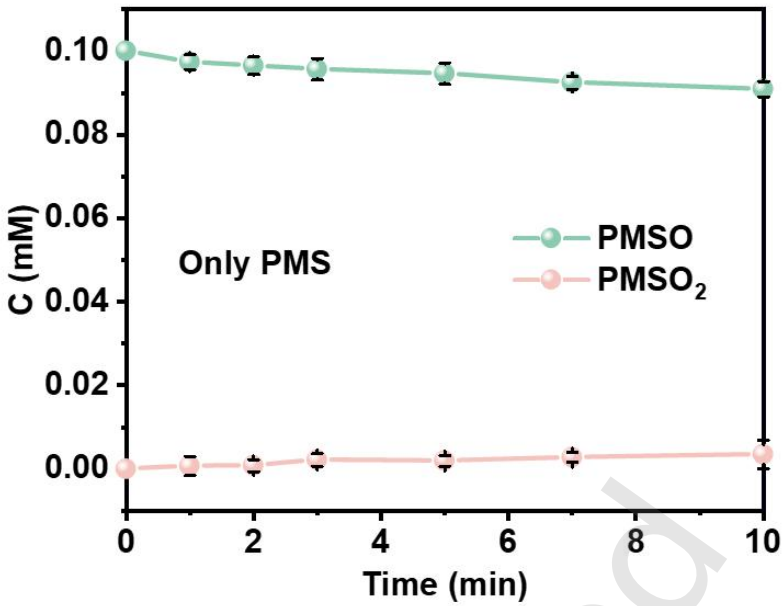


Fig. S26. Consumption of PMSO and generation of $PMSO_2$ in the PMS/PMSO system.

Just Accepted

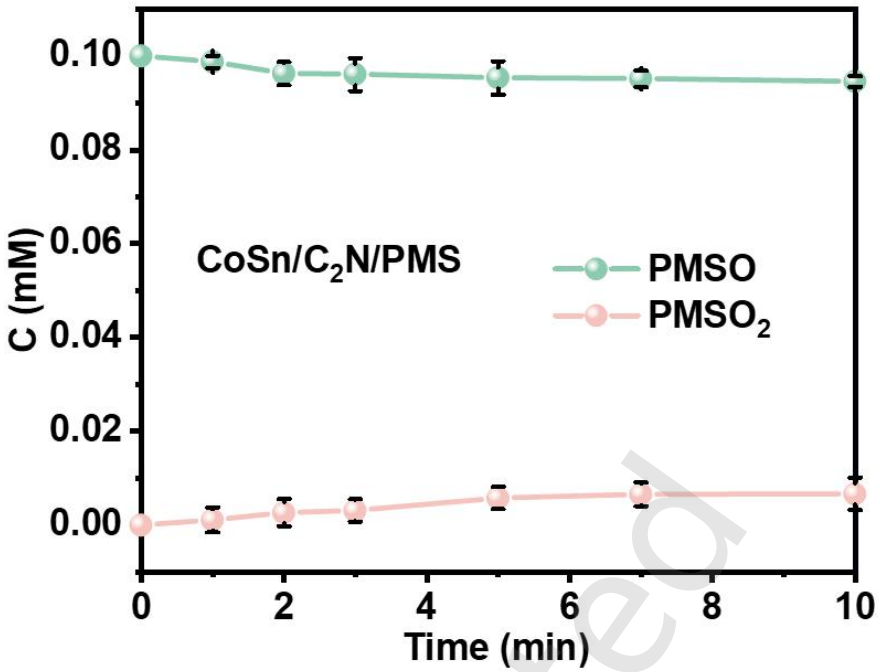


Fig. S27. Consumption of PMSO and generation of $PMSO_2$ in the $CoSn/C_2N$/PMS/PMSO system.

Just Accepted

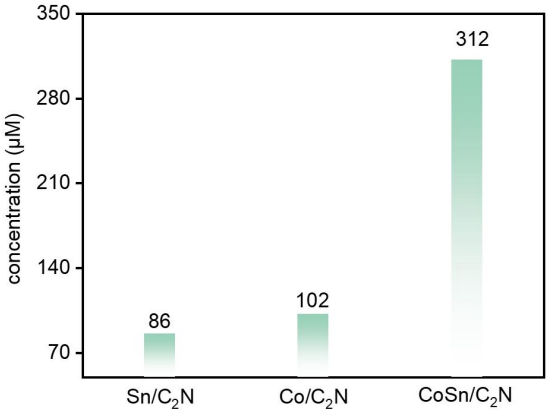


Figure S28. Different ROS yields in Sn/C_2N, Co/C_2N and $CoSn/C_2N$ systems.

Just Accepted

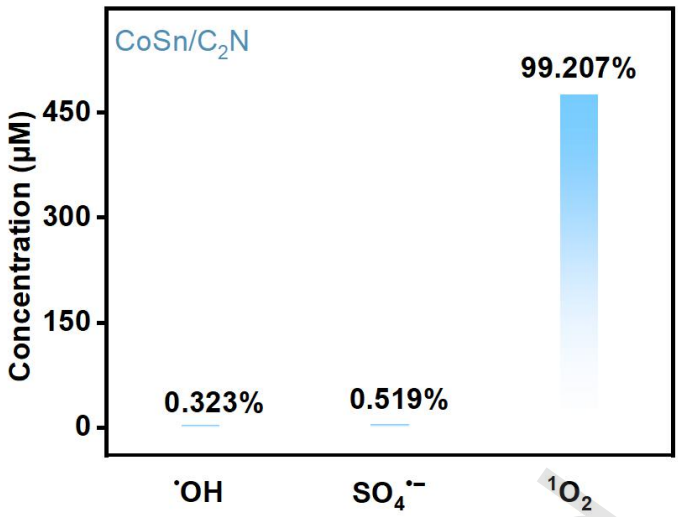
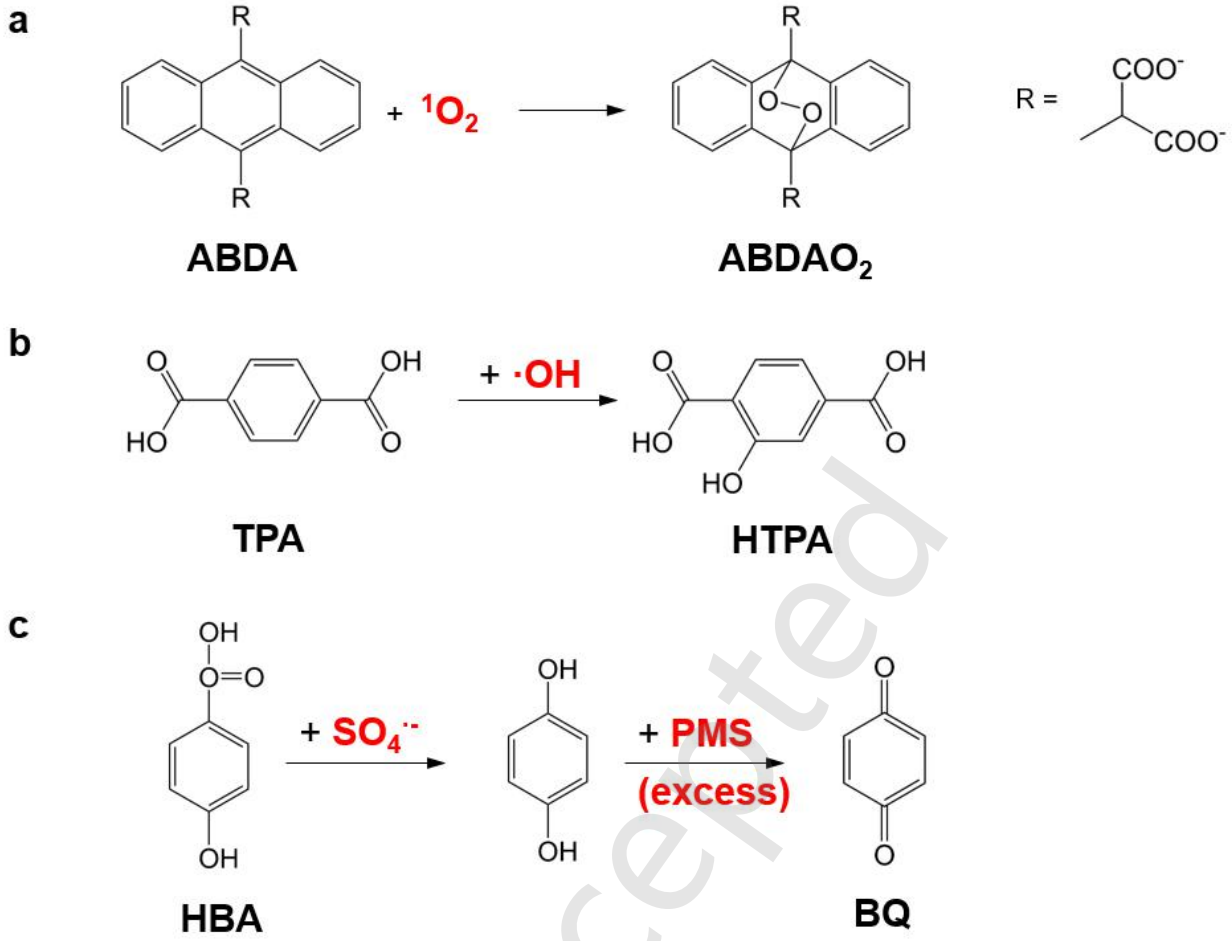


Figure S29. Quantitative analysis of ROS in the $CoSn/C_2N$/PMS system

Just Accepted



Just Accepted

Figure S30. Chemical equation of (a) 9,10-anthracene-diyl-bis(methylene) dimalonic acid and $^1O_2$, (b) terephthalic acid and $^{\bullet}OH$, and (c) p-Hydroxybenzonic acid and $SO_4^{\bullet-}$.

Quantitative $^1O_2$: Solution test with UV-Vis absorbance measurement for $^1O_2$ detection. UV-Vis spectra were recorded using a Jasco V-750 spectrophotometer. The chemical probe 9,10-anthracene-diyl-bis(methylene) dimalonic acid (ABDA) was employed for the detection of $^1O_2$. Initially, an ABDA indicator solution with a concentration of 1 mg/mL was prepared. Since the catalyst itself exhibits absorption characteristics, 10 mg of Co-ACN or Co-CCN was fully dispersed in 95 mL of deionized water before measurement. The baseline was first recorded, and then 5 mL ABDA was added to the reaction system. The UV-Vis spectra were measured at various reaction times, and the concentration of $^1O_2$ was calculated according to the standard curve.

Quantitative $SO_4^{\bullet-}$: The amount of $SO_4^{\bullet-}$ generated in the Co-ACN/PMS or Co-CCN/PMS system was detected using p-Hydroxybenzonic acid (HBA) as a chemical probe. Based on the reaction stoichiometry, 1 mol of HBA reacts with 1 mol of $SO_4^{\bullet-}$ to form hydroquinone which is immediately transformed to a stable by product, namely 1,4-Benzoquinone (BQ) by the excess PMS. Ultimately, the BQ in the system is detected by HPLC and the concentration of $SO_4^{\bullet-}$ can be determined after conversion.

Quantitative $^{\bullet}OH$: The concentration of $^{\bullet}OH$ generated during the AOP process is quantified by Liquid photoluminescence (PL) Spectra. Terephthalic acid (TPA) can capture $^{\bullet}OH$ to form 2-hydroxyterephthalic acid (HTPA) with strong fluorescent signal. The quantification system was consistent with the degradation experiments except that benzoic acid was used instead of pollutants ([catalyst] = 0.1 L^{-1}; [Temp] = 25 °C; initial pH = 7.0 ± 0.2). After adsorption for 30 min to reach equilibrium, PMS was added to the reaction system (the concentration of PMS in the system was 0.075 mM). The solution is collected at intervals, filtered, and then measured by PL emission spectroscopy at excitation wavelength of 330 nm.

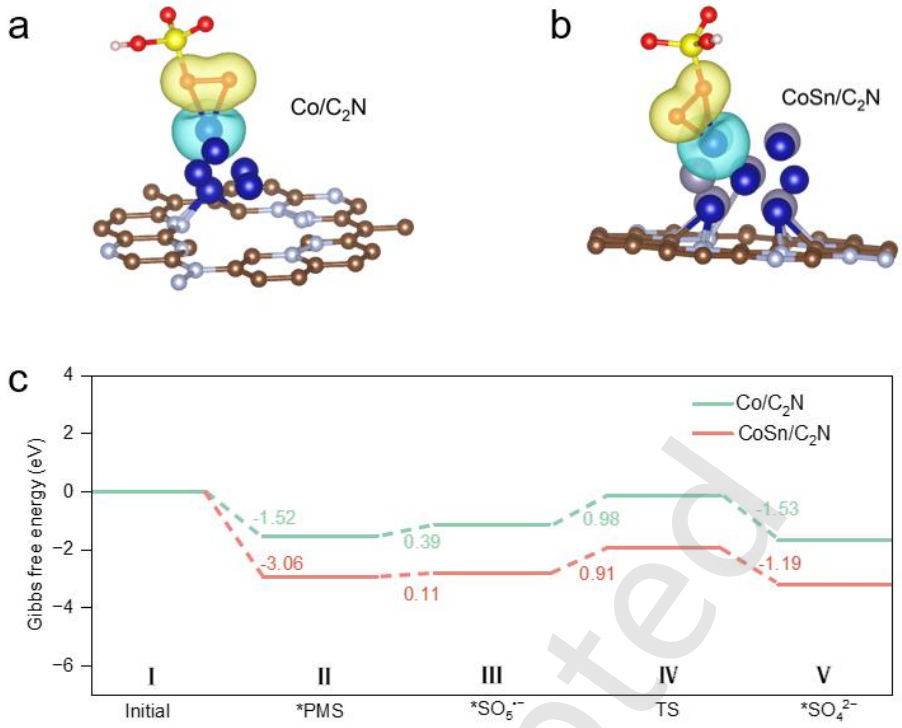


Fig. S31. (a) Differential charge density diagram of PMS adsorbed on the Co/C_2N model; (b) Differential charge density diagram of PMS adsorbed on the $CoSn/C_2N$ model; (c) Gibbs free energy profiles for PMS activation on Co/C_2N and $CoSn/C_2N$.

Just Accepted

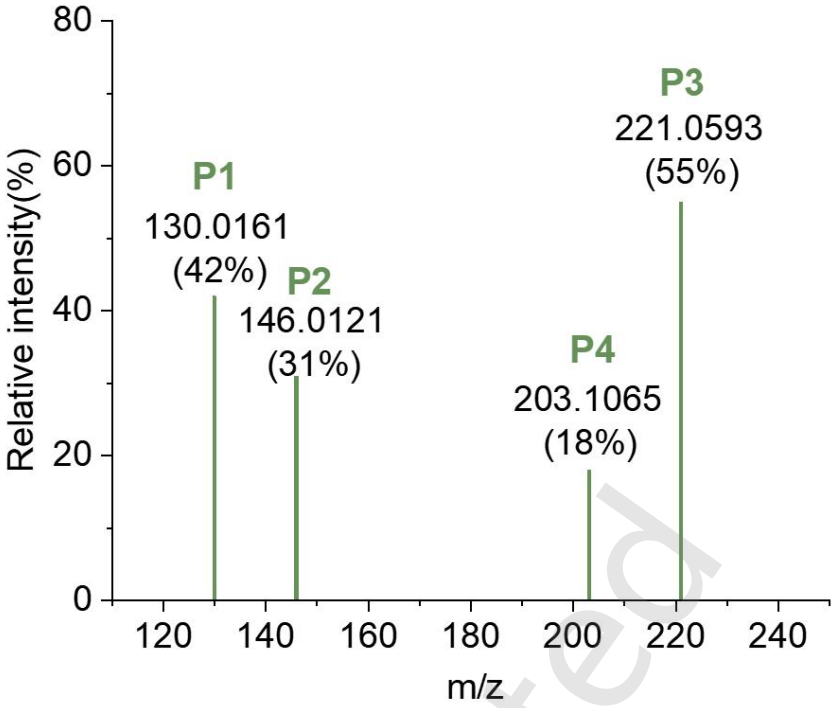


Figure S32. Illustrative LC-MS spectrum of SCP transformation products.

Just Accepted

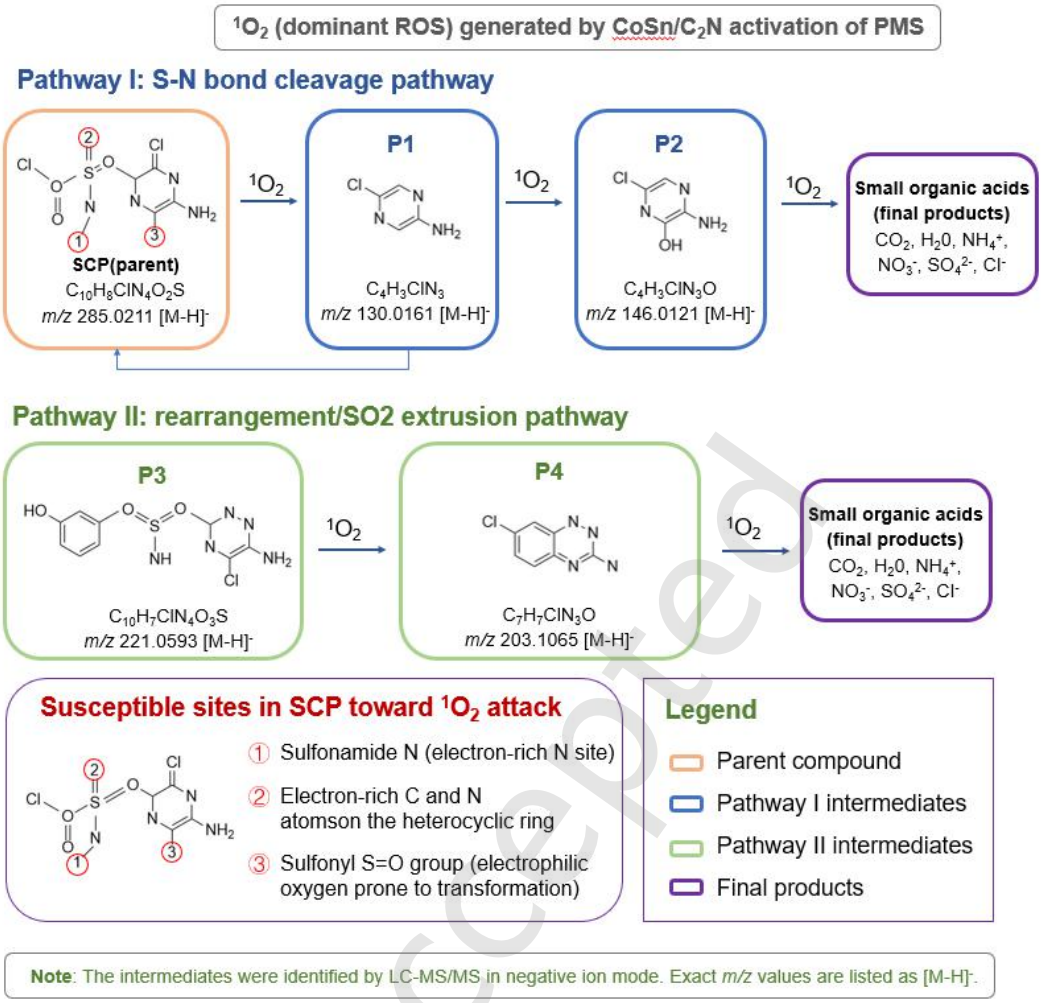


Figure S33. Proposed non-radical $^1O_{22}$-mediated degradation pathways of SCP and LC-MS identified intermediates.

Just Accepted

Table S1. Structural parameters extracted from the Co K-edge EXAFS fitting. (S_0^2=0.85)

sample	Path	CN	R(Å)	$\sigma^2(10^{-3}Å^2)$	ΔE_0(eV)	R factor
Co foil	Co-Co	12*	2.49±0.01	4.2±0.5	5.6±0.6	0.006
$CoSn/C_2N$	Co-N	2.5±0.3	2.04±0.02	4.8±0.3	2.5±0.1	0.011
	Co-Co/Sn	2.3±0.1	3.02±0.02	5.5±0.6		
Co/C_2N	Co-N	2.1±0.1	2.05±0.01	5.1±0.5	3.2±0.3	0.009
	Co-Co	2.0±0.2	2.48±0.02	6.3±0.8		

S_0^2 was the amplitude reduction factor; CN was the coordination number; R was interatomic distance (the bond length between Co central atoms and surrounding coordination atoms); σ^2 was Debye-Waller factor (a measure of thermal and static disorder in absorber-scatterer distances); ΔE_0 was the edge-energy shift (the difference between the zero kinetic energy value of the sample and that of the theoretical model). R factor was used to value the goodness of the fitting.

* This value was fixed during EXAFS fitting, based on the known structure.

Just Accepted

Table S2. Structural parameters extracted from the Sn K-edge EXAFS fitting. (S_0^2=0.89)

sample	Path	CN	R(Å)	$\sigma^2(10^{-3}Å^2)$	ΔE_0(eV)	R factor
Sn foil	Sn-Sn	12.0*	2.98±0.02	5.3±0.3	4.1±0.5	0.006
$CoSn/C_2N$	Sn-N	2.3±0.2	2.01±0.01	4.4±0.5	3.2±0.2	0.011
	Sn-Co/Sn	3.1±0.3	3.01±0.02	5.3±0.2		

S_0^2 was the amplitude reduction factor; CN was the coordination number; R was interatomic distance (the bond length between Sn central atoms and surrounding coordination atoms); σ^2 was Debye-Waller factor (a measure of thermal and static disorder in absorber-scatterer distances); ΔE_0 was the edge-energy shift (the difference between the zero kinetic energy value of the sample and that of the theoretical model). R factor was used to value the goodness of the fitting.

* This value was fixed during EXAFS fitting, based on the known structure.

Just Accepted

Catalyst ($g \cdot L^{-1}$)	Pollutant (mM)	PMS (mM)	k_1 (min^{-1})	K_1 ($L \cdot min^{-1} g^{-1}$)	References
$CoSn/C_2N$ (0.1)	**SCP(0.07)**	**0.1**	**0.249**	**1.743**	**This work**
$CoPc/G\text{-}NH_2$ (0.02)	Phenol (0.01)	0.2	0.226	0.565	[1]
$Fe–Co–O–g\text{-}C_3N_4$ (0.2)	SMX (0.04)	0.2	0.085	0.02125	[2]
$Co\text{-}N_2$ (0.2)	BPA (0.05)	2	0.695	0.086875	[3]
$Cu\text{-}N_4/C\text{-}B$ (0.1)	BPA (0.09)	0.65	0.56	0.77538462	[4]
Cu-rGo LDH (0.25)	BPA (0.09)	3	0.046	0.00552	[5]
$Mn_{SA}–N–C_{O,S}$ (0.2)	BPA (0.04)	2	0.36	0.036	[6]
Fe-Co-DAC (0.2)	BPA (0.08)	0.4	0.23	0.23	[7]
$Co\text{-}N_3O_1$ (0.1)	CIP (0.002)	1	1.15	0.23	[8]
FeCo-NCB (0.1)	BPA (0.05)	0.5	0.659	0.659	[9]
$Ru_n/NC\text{-}850$ (0.02)	CIP (0.004)	1	0.08	0.008	[10]

Table S3. Degradation efficiency of pollutants by different catalysts.

Just Accepted

References

[1] B. Huang, X. Ren, J. Zhao, Z. Wu, X. Wang, X. Song, X. Li, B. Liu, Z. Xiong, B. Lai, Modulating Electronic Structure Engineering of Atomically Dispersed Cobalt Catalyst in Fenton-like Reaction for Efficient Degradation of Organic Pollutants. *Environ. Sci. Technol.* **2023**, *57*, 14071-14081.

[2] S. Wang, J. Wang, Peroxymonosulfate activation by Co_9S_8@ S and N co-doped biochar for sulfamethoxazole degradation. *Chem. Eng. J.* **2020**, *385,* 123933.

[3] X. Liang, D. Wang, Z. Zhao, T. Li, Y. Gao, C. Hu, Coordination Number Dependent Catalytic Activity of Single-Atom Cobalt Catalysts for Fenton-Like Reaction. *Adv. Funct. Mater.* **2022**, *32,* 2203001.

[4] X. Zhou, M.-K. Ke, G.-X. Huang, C. Chen, W. Chen, K. Liang, Y. Qu, J. Yang, Y. Wang, F. Li, H.-Q. Yu, Y. Wu, Identification of Fenton-like active Cu sites by heteroatom modulation of electronic density. *Proc. Natl. Acad. Sci. U.S.A.* **2022**, *119(8),* e2119492119.

[5] A. Shahzad, J. Ali, J. Ifthikar, G. G. Aregay, J. Zhu, Z. Chen, Z. Chen, *J.* Non-radical PMS activation by the nanohybrid material with periodic confinement of reduced graphene oxide (rGO) and Cu hydroxides. *Hazard. Mater.* **2020**, *392,* 122316.

[6] X. Fu, Q. Zeng, Y. Gao, L. Song, Y. Wen, T. Cai, Q. Zhang, C. Hu, Q. Zeng, Single-Atom Mn–N4 Catalyst with Electron-Rich O and S Self-Doping for Cooperative Nonradical and Radical Oxidation: Overlooked Nonmetal Heteroatomic Sites. *ACS ES&T Eng.* **2024**, *4*, 903-914.

[7] F. Wang, Y. Gao, H. Fu, S.-S. Liu, Y. Wei, P. Wang, C. Zhao, J.-F. Wang, C.-C. Wang, Almost 100% electron transfer regime over Fe– Co dual-atom catalyst toward pollutants removal: Regulation of peroxymonosulfate adsorption mode. *Appl. Catal. B* **2023**, *339*, 123178.

[8] Z. Wang, E. Almatrafi, H. Wang, H. Qin, W. Wang, L. Du, S. Chen, G. Zeng, P. Xu, Cobalt Single Atoms Anchored on Oxygen-Doped Tubular Carbon Nitride for Efficient Peroxymonosulfate Activation: Simultaneous Coordination Structure and Morphology Modulation, *Angew. Chem. Int. Ed.* **2022**, *61*, e202202338.

[9] S. Liu, J. Du, H. Wang, W. Jia, Y. Wu, P. Qi, S. Zhan, Q. Wu, J. Ma, N. Ren, W.-Q. Guo, How hetero-single-atom dispersion reconstructed electronic structure of carbon materials and regulated Fenton-like oxidation pathways. *Water Res.* **2024**, *254*, 121417.

[10] G. Bi, R. Ding, J. Song, M. Luo, H. Zhang, M. Liu, D. Huang, Y. Mu, Discriminating the Active Ru Species Towards the Selective Generation of Singlet Oxygen from Peroxymonosulfate: Nanoparticles Surpass Single-Atom Catalysts. *Angew. Chem. Int. Ed.* **2024**, *63*, e202401551.

Just Accepted